


FULL PAPER

Open Access



# Reduction of non-tidal oceanographic fluctuations in ocean-bottom pressure records of DONET using principal component analysis to enhance transient tectonic detectability

Hideto Otsuka<sup>1\*</sup> , Yusaku Ohta<sup>1</sup>, Ryota Hino<sup>1</sup>, Tatsuya Kubota<sup>2</sup>, Daisuke Inazu<sup>3</sup>, Tomohiro Inoue<sup>4,5</sup> and Narumi Takahashi<sup>2,6</sup>

## Abstract

Ocean bottom pressure-gauge (OBP) records play an essential role in seafloor geodesy. Oceanographic fluctuations in OBP data, however, pose as a significant noise source in seafloor transient crustal deformation observations, including slow slip events (SSEs), making it crucial to evaluate them quantitatively. To extract the significant fluctuation phenomena common to multiple observation networks, including oceanographic fluctuations and tectonic signals, we applied principal component analysis (PCA) to the 3-year Dense Oceanfloor Network System for Earthquakes and Tsunamis (DONET) OBP time series for 40 stations during 2016–2019. PCA could separate several oceanographic signals based on the characteristics of their spatial distributions, although evident transient tectonic signals could not be confirmed from the observed pressure records during this observed period. The spatial distribution of the first four principal components (PCs) reflected the common component, inclined component along sea depth, longitude component, and parabola-like pattern, respectively. By subtracting each PC (in particular, PC-2 and PC-4) from the time series, we could significantly reduce the sea depth dependence of OBP records, which has been highlighted in several previous studies and is also evident in this region. We interpreted PCs 2–4 as the reflection of the strength and meandering of ocean geostrophic currents based on a comparison with the PC spatial distribution of the numerical oceanographic models. In addition, to evaluate the ability of PCA to separate transient tectonic signal from OBP time series, including oceanographic fluctuations, we conducted a synthetic ramp assuming an SSE by rectangular fault and then applied PCA. The assumed synthetic tectonic signal could be separated from the oceanographic signals and included in the principal component independently depending on its amplitude, suggesting that the spatial distribution of each PC would change if the amplitude of the synthetic signal were sufficiently large. We propose a transient event-detection method based on the spatial distribution difference of a specific PC with or without a tectonic signal. We used the normalized inner product (NIP) between these PCs as the indicator of their similarities. This method can detect transient tectonic signals more significantly than the moment-magnitude scale of 5.9 from OBP records.

**Keywords** DONET, Nankai trough, Ocean bottom pressure-gauge, Oceanographic fluctuations, Principal component analysis, Seafloor crustal deformation, Slow slip events

\*Correspondence:

Hideto Otsuka

hideto.otsuka.q6@dc.tohoku.ac.jp

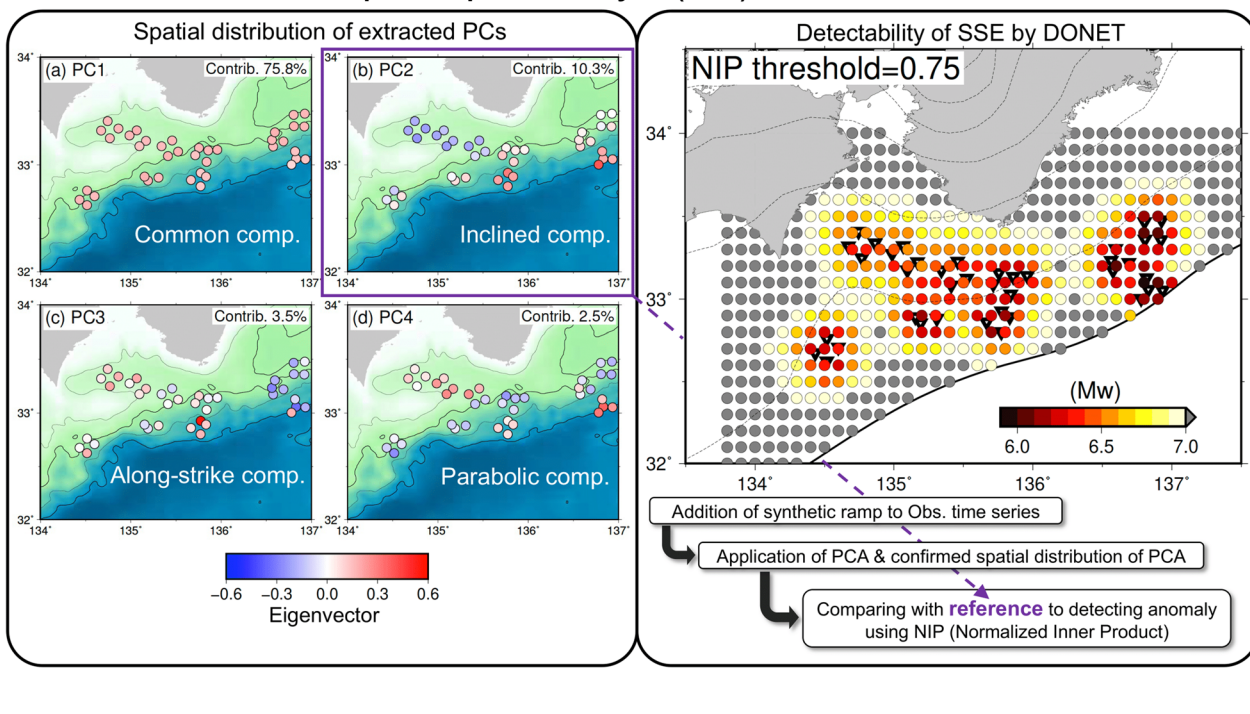
Full list of author information is available at the end of the article



© The Author(s) 2023. **Open Access** This article is licensed under a Creative Commons Attribution 4.0 International License, which permits use, sharing, adaptation, distribution and reproduction in any medium or format, as long as you give appropriate credit to the original author(s) and the source, provide a link to the Creative Commons licence, and indicate if changes were made. The images or other third party material in this article are included in the article's Creative Commons licence, unless indicated otherwise in a credit line to the material. If material is not included in the article's Creative Commons licence and your intended use is not permitted by statutory regulation or exceeds the permitted use, you will need to obtain permission directly from the copyright holder. To view a copy of this licence, visit <http://creativecommons.org/licenses/by/4.0/>.

Graphical Abstract

Principal Component Analysis (PCA) for DONET OBPs



Main Text

Introduction

Seafloor geodetic observations are critical for accurately understanding crustal deformation associated with phenomena such as transient fault slips (e.g., Bürgmann and Chadwell 2014). Among the seafloor geodetic instruments, the ocean bottom pressure-gauge (OBP) is a sensor that can continuously monitor vertical crustal deformation of the seafloor and tsunamis over a broad range of time scales and has been the subject of many previous studies (Ohta et al. 2012; Tsushima et al. 2012; Ito et al. 2013; Suzuki et al. 2016; Wallace et al. 2016; Sato et al. 2017; Fukao et al. 2021; Kubota et al. 2021; Woods et al. 2022). However, the water-pressure time series obtained by the OBP includes various components such as tidal impacts, instrumental drift, non-tidal oceanographic fluctuations, and crustal deformation, making it extremely important to address these influences for extracting objective crustal deformation components. Particularly, the non-tidal oceanographic fluctuation component has a characteristic time constant of more than a few days (Dobashi and Inazu 2021), and the time constants are similar to those of slow slip events (SSEs), resulting in transient crustal deformation events (e.g., Obara and Kato 2016; Rousset et al. 2017; Takagi

et al. 2019; Okada et al. 2022). Thus, appropriate estimation and removal of non-tidal oceanographic fluctuation components are critical for accurately identifying the tectonic components. Such non-tidal oceanographic components can be removed by applying a bandpass filter to eliminate oceanic origins, excluding specific constants (Suzuki et al. 2016; Wallace et al. 2016; Sato et al. 2017; Muramoto et al. 2019), and using a physical model to calculate the expected pressure fluctuation values and subtract them from the observed time series (Inazu et al. 2012; Dobashi and Inazu 2021). Although these methods can improve the signal-to-noise ratio of non-tidal oceanographic fluctuations, their spatiotemporal characterization is required to enable the detection of smaller tectonic-induced pressure changes.

The spatiotemporal characteristics of these non-tidal oceanographic components recorded in the OBP have been identified in several previous studies. Muramoto et al. (2019) found that the oceanographic fluctuations recorded in the OBP time series off-Hikurangi, New Zealand [Hikurangi Ocean Bottom Investigation of Tremor and Slow Slip (HOBITSS), which extends up to approximately 60 km square (Wallace et al. 2016)], became less similar with an increase in the difference in sea depths between OBP sites increased. Inoue et al. (2021) used

the standard deviation of the relative pressure time series between stations in the same observational network and observation period as Muramoto et al. (2019) to evaluate similarities in the time series based on the station distance and sea-depth differences. These studies showed that the depth dependence was more significant than the station distance in the OBP time series. However, the larger spatial characteristics of these non-tidal oceanographic fluctuation components still need to be investigated. Moreover, the currently available interpretations and discussions of the similarities of these features at comparable sea depths are also insufficient.

Principal component analysis (PCA) (Jolliffe 2002) is a standard technique for analyzing large datasets containing a high number of dimensions/features per observation, increasing the interpretability of data while preserving the maximum amount of information. PCA has been employed in land-based geodesy (Kositsky and Avouac 2010; Munekane 2012), seafloor geodesy (Hino et al. 2014, 2022; Gomberg et al. 2019; Fredrickson et al. 2023), oceanography (e.g., Kutzbach 1967; Kundu et al. 1975; Androsov et al. 2020), and other fields to evaluate and remove common modes. Hino et al. (2014) applied

PCA to the OBP time series and showed that it could remove non-tidal oceanographic fluctuation components common to the entire OBP network. They demonstrated that the signal-to-noise ratio of the OBP time series could be improved by removing the first principal component (PC). Watts et al. (2021) and Fredrickson et al. (2023) applied complex PCA (Thomson and Emery 2014; Nuryanto 2016), which can also evaluate propagation components by extending PCA to complex numbers, to four OBP time series stations and evaluated its performance with respect to removing oceanographic components from the OBP time series. These previous studies showed that PCA effectively removes non-tidal oceanographic fluctuations from the OBP time series but lacks a spatiotemporal assessment of each extracted component.

Given this research background, this study focused on the OBP observation network in the Dense Ocean-floor Network system for Earthquakes and Tsunamis (DONET; Fig. 1) (Kaneda et al. 2015; Kawaguchi et al. 2015) in southwest Japan, where the observational network is densely and widely distributed. In the Nankai Trough region, where the DONET is installed, the transient SSEs have often been observed and their

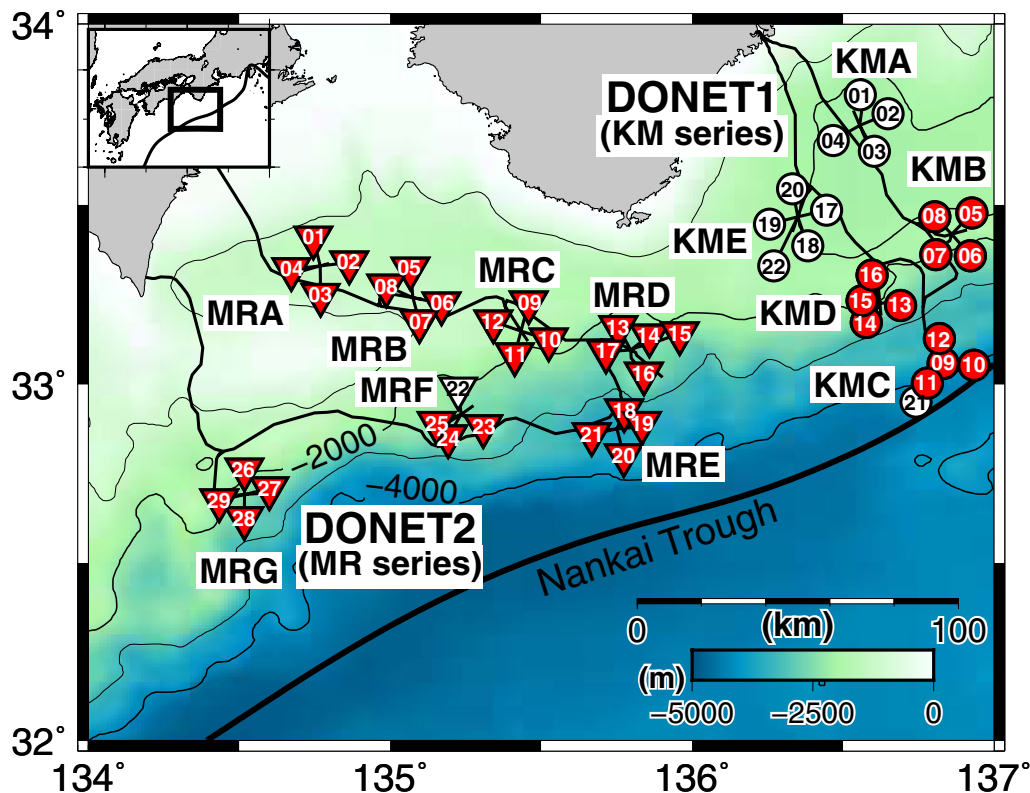


**Fig. 1** DONET observatory site map. Circles and triangles indicate the DONET1 and DONET2 observation sites, respectively. A group of four or five observation sites is a “node,” and the node name is shown in the vicinity of each node. For example, the name of the westernmost site is MRG29. The red-colored sites have been used for our principal component analysis. The bold black line indicates the Nankai Trough (Iwasaki et al. 2015)

spatiotemporal variations have been extensively studied (Obara and Kato 2016; Araki et al. 2017; Yokota and Ishikawa 2020; Ariyoshi et al. 2021). Owing to the long-term continuous observations and the spatial extent of the DONET data, we can now quantify the spatial characteristics of non-tidal oceanographic fluctuations in further detail and evaluate the ability of PCA to separate tectonic and oceanographic signals, which has not been carried out in previous studies. Therefore, we applied PCA to the long-term time series of the DONET data and examined its spatiotemporal characteristics. Furthermore, we have discussed the possibility of applying PCA to data in which transient crustal deformations are included in the OBP time series to separate these features from the time series. We further propose a transient event-detection method based on the spatial distribution variation of a specific PC.

**Seafloor pressure data and data processing**

We used OBP data acquired via a cabled seismic observation system named DONET in the Nankai Trough of southwestern Japan. The DONET observatory includes an accelerometer, broadband seismometer, pressure sensor, hydrophone, and thermometer, among others, to observe the seafloor conditions. Absolute quartz oscillation pressure sensors, with a sampling frequency of 10 Hz, by Paroscientific, Inc., were used as pressure sensors (Matsumoto and Araki 2021). The DONET observatory consists of two cables with several nodes that group four or five observational sites in the vicinity (Fig. 1). The eastern cable (DONET1, KMA to KME nodes; 22 stations) began monitoring in 2011, while the western cable (DONET2, MRA to MRG nodes; 29 stations) in 2016 (Fig. 2). For instance, the KMA node includes the KMA01–KMA04 stations and the MRF node includes the MRF22–MRF25 stations (Fig. 2). To ensure a sufficient time series data length, 40 sites from June 2, 2016,

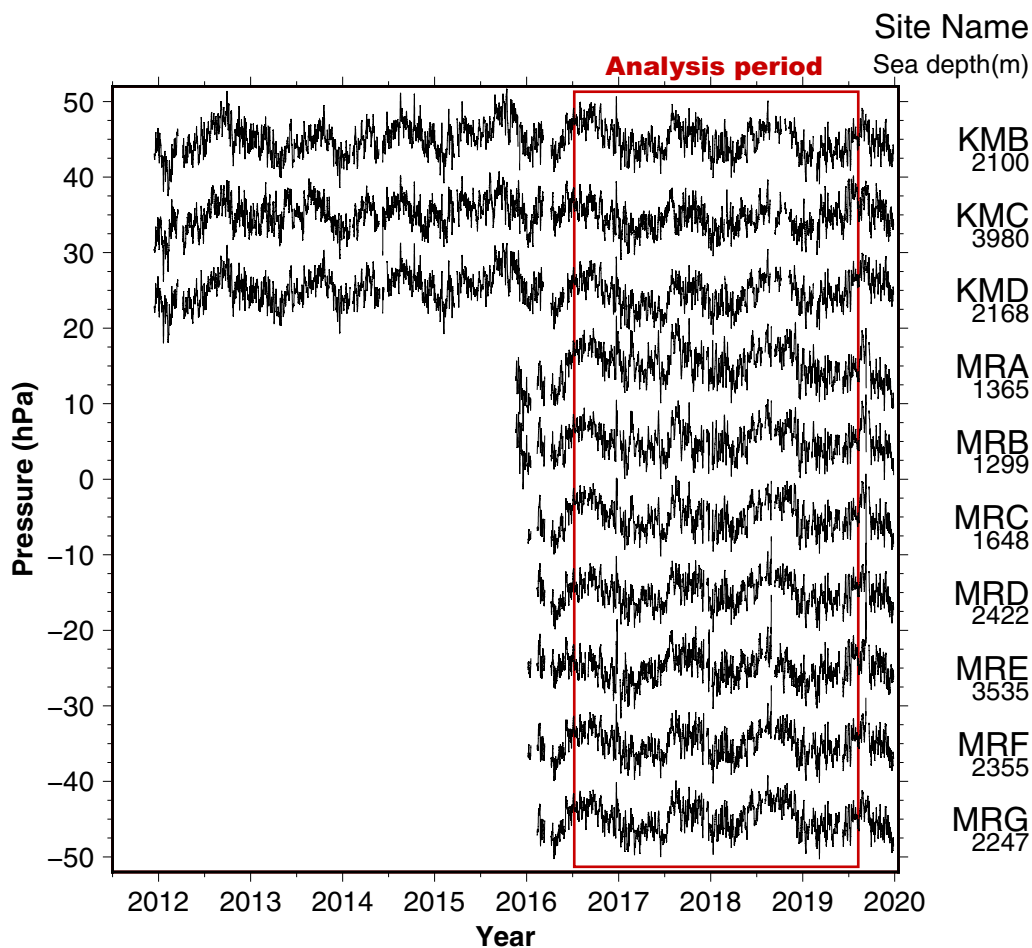


**Fig. 2** Averaged 8-year long-term continuous OBP time series for each node. The red rectangle indicates the analysis period in this study. The node name and the average sea depth of each node are shown on the right side of the figure

to August 12, 2019, with few missing measurements, were used for the analysis (Fig. 1). The pressure data for all the KMA sites and MRF22 were unavailable post-October 2018 and March 2018, respectively. No data for the KME sites were available during the analysis period.

The OBP time series contains signals other than the targeted crustal deformation. The observed OBP time series can be described by Eq. 1 (Ito et al. 2013; Hino et al. 2014):

$$\Delta p_B(t) = \Delta p_C(t) + \Delta p_T(t) + \Delta p_O(t) + \Delta p_D(t) + \varepsilon(t), \quad (1)$$

where  $\Delta p_B(t)$ ,  $\Delta p_C(t)$ ,  $\Delta p_T(t)$ ,  $\Delta p_O(t)$ ,  $\Delta p_D(t)$ , and  $\varepsilon(t)$  represent the observed pressure, crustal deformation, tidal signal, non-tidal oceanographic fluctuations, instrumental drift, and other errors, respectively. The following procedure was used to extract the crustal deformation component from the OBP time series.

The original 10 Hz sampling data were down-sampled by averaging them over one hour. The missing parts were linearly interpolated to use the tide-killer filter as follows: the tidal component ( $\Delta p_T(t)$ ) was removed using a low-pass filter designed for removing tidal components (the 48-h tide-killer filter designed by Hanawa and Mitsudera 1985). This tide-killer filter extended the Thompson (1983) filter to 48 h. It uses a 10-day weighted moving average to reduce the filter response factor to approximately zero in less than 2 days [for the weighting factor, see Table 3 by Hanawa and Mitsudera (1985)]. The weighting factors of this filter were adjusted so that the inertial motions contained in tidal currents and other oceanographic phenomena near Japan could also be removed. Bayesian Tidal Analysis Program -Grouping Model program (BAYTAP-G) (Tamura et al. 1991) is often used to estimate and remove tidal variations from OBP time series; however, small fluctuations with a high frequency (time constant of fewer than 2 days) remain in the time series. As this study pertains to crustal deformations in the range of a few days or more, high-frequency variations are outside the scope of this study. Therefore, a simple low-pass filter was applied. The tide-killer filter produces inappropriate variability when applied to a time series that does not include tidal variations. Hence, the missing parts and the time series for the 5 days before and after the missing periods were removed prior to the instrumental drift estimation. The instrumental drift component ( $\Delta p_T(t)$ ) was estimated and removed using linear and exponential approximations (Watts and Kontoyianis 1990; Polster et al. 2009); the averaged drift rate over the stations was approximately several hPa per year. The instrumental drift was estimated using the time series for all time periods that existed before the end of 2019 (i.e., almost all DONET1 stations operated during 2012–2019, and all DONET2 and KMC21 operated during 2016–2019)

for more accurate estimation. The missing part of the time series was re-interpolated using a piecewise cubic Hermite interpolating polynomial (Fritsch and Carlson 1980). Processed data, in which tectonic and oceanographic signals were retained, were used in the following analyses. These processed data have, henceforth, been called “observed data.”

### Principal component analysis for processed time series

We assumed that the observed data contained multiple spatially correlated non-tidal oceanographic fluctuation signals that could be separated by PCA, a major multivariate analysis method that uses as few synthetic variables as possible to capture as much information (Jolliffe 2002). We applied PCA to the observed data to extract non-tidal oceanographic components with spatial similarities from the OBP time series. This study first applied PCA to a long-term OBP data set to extract non-tidal oceanographic components to acquire crustal deformation data. We adopted the conventional PCA method for the preprocessed observed data. For each extracted PC, an assessment was made on whether the component should be attributed to the non-tidal oceanographic contribution based on its spatial characteristics.

As mentioned in the introduction, the oceanographic fluctuations in the OBP data are sea-depth dependent (Fredrickson et al. 2019; Inoue et al. 2021). To confirm these PCA effects and the subsequent selection and removal of PCs, the relative pressure between sites in the OBP time series and their dependence on the difference in distance and sea depth were calculated. For each site, variations from an assumed reference site and standard deviation (SD) of the relative water-pressure time series were determined, along with the evaluation of the dependence on distance and sea depth between those stations. In this study, we used the absolute averaged SD for overall stations (ASD) and the relative SD for each station (RSD) to explain the PCA contributions shown below. We calculated ASD and RSD for the 10 types of time series: (1) time series of observed pressure, (2) first PC (PC-1), (3) second PC (PC-2), (4) third PC (PC-3), (5) fourth PC (PC-4), (6) the observed pressure after subtracting PC-1, (7) after subtracting PCs 1 and 2, (8) after subtracting PCs 1–3, (9) after subtracting PCs 1, 2, and 4, and (10) after subtracting PCs 1–4. The ASD for the time series types of  $l$  is shown in Eq. 2:

$$ASD^l = \frac{1}{N} \sum_{i=1}^N \sqrt{\frac{1}{T} \sum_{t=1}^T (P_{i,l}^t - \overline{P_{i,l}})^2} \quad (2)$$

where  $P_{i,l}^t$  indicates the pressure for the time series type of  $l$  at time  $t$  at station  $i$ , and  $\overline{P_{i,l}}$  denotes the temporal

average of  $P_{i,l}^t$ . The RSD at station  $i$  from the reference station  $j$  is shown in Eq. 3:

$$RSD_{ij}^l = \sqrt{\frac{1}{T} \sum_{t=1}^T \left\{ \left( P_{i,l}^t - P_{j,l}^t \right) - \left( \overline{P_{i,l}} - \overline{P_{j,l}} \right) \right\}^2}, \quad (3)$$

where  $P_{i,l}^t$  and  $P_{j,l}^t$  indicate the pressure record for the time series type of  $l$  at time  $t$  at station  $i$  and  $j$ , respectively.  $\overline{P_{i,l}} - \overline{P_{j,l}}$  denotes the average relative pressure time series between station  $i$  and  $j$ .

### Spatiotemporal characteristics of OBP time series

Figure 2 shows an example of the OBP time series after removing the tidal and drift components from the observed time series. These time series indicate annual variations: a higher-pressure value appeared in the summer season (July to August) and a lower pressure value appeared in the winter season (January to February). This annual variation was evident even before 2016 in the DONET1 network (KMB–KMD time series) prior to our analysis period (Fig. 2). The annual variation has an amplitude of up to 5 hPa, and these characteristics are within the same node and display similar features over a wide area (Additional file 1: Fig. S1). Similar characteristics can be observed throughout the network, even for shorter time-constant variations. In the following sections, we present the PCA results that separate these spatially coherent oceanographic fluctuations.

### Spatiotemporal characteristics of each principal component

In PCA, PC-1 has the largest eigenvalue. PC-1 is more highly correlated with the original features than PC-2, while PC-2 is better correlated than PC-3, and so on. PCA reduces the dimensionality of the data by selecting the first  $k$  PCs to represent the original data. Figure 3a–d shows the extracted PCs at the DONET OBP sites. The eigenvector and eigenscore of each PC correspond to its spatial distribution and temporal variation, respectively. The contributions of each PC were 75.8% for PC-1, 10.3% for PC-2, 3.5% for PC-3, and 2.5% for PC-4 (Fig. 3). The cumulative contribution reached 92% through PCs 1–4, and the spatial patterns and other characteristics of the higher-order components after PC-5 were not clear; therefore, the sections hereafter will utilize PCs 1–4 to interpret their characteristics. PC-1 and PC-2 explain the majority (86.1%) of the time series characteristics; PC-1 is the common component across the entire observational network and includes the annual variability (Figs. 3a and 4a). PC-2 has a spatially inclined characteristic, reversing the positive and negative eigenvector values between shallow and deep stations (Figs. 3b and 4c).

This sea depth dependence characteristic is clear in the time series of PC-2, whose amplitude is notably large in shallow or deep stations (Figs. 5b). PC-3 does not have a clear sea-depth dependency like PC-2, but it does have a longitudinal dependence characteristic (Figs. 3c and 4f). PC-4 has parabolic spatial characteristics with positive and negative eigenvector values at shallow and deep-water depths, respectively (Figs. 3d and 4g). Based on the characteristics of each of these PCs, PCs 1–4 were determined to be the components that needed to be removed from the oceanographic fluctuation components in this study.

Previous studies have noted the sea-depth dependency of the seafloor water-pressure characteristics based on actual observed data and oceanographic models (Fredrickson et al. 2019; Inoue et al. 2021). The PCA results obtained in this study were consistent with those of previous studies. Our results also suggest that the depth-dependent component can not only be extracted as the main component but also be separated into two different components: PC-2 and PC-4.

### Contribution of the PCs in the OBP time series

The results of the subtraction of the PCs from the original observed data in different combinations were evaluated to confirm how the noise in the OBP time series can be reduced using the extracted PCs (Fig. 6). After removing PC-1 (Fig. 5a), which included the annual variation component, the ASD of the time series was considerably reduced from 1.98 hPa to 0.91 hPa (the ASD value was reduced by 46%), while the spatially correlated variations remained (Fig. 6b). The characteristics of the remaining components are not common to the entire observational network but are identified at specific sites, which suggests that they reflect depth-dependent oceanographic fluctuations. Figure 6c shows the results of subtracting PC-1 and PC-2 from the observed data. Figure 6c depicts the elimination of the remaining variations, where the ASD shows a decrease to 0.69 hPa (the ASD value was further reduced by 24%, for an overall reduction of 65%). By removing PCs 1–3, the ASD decreased to 0.61 hPa (Additional file 1: Fig. S2b), and removing PCs 1, 2, and 4 resulted in an ASD of 0.62 hPa (Additional file 1: Fig. S2c). Finally, removing PCs 1–4 resulted in an ASD of 0.53 hPa (Additional file 1: Fig. S2d), reducing the noise level by 73% compared to the time series prior to the removal of PCs. PCA is a method of identifying as much information as possible using as few synthetic variables. Naturally, subtracting the PCs with high contributions from the original data reduces their noise levels; however, as previously mentioned, PCs 1–4 showed distinct spatially correlated variations that could be attributed to oceanic origins. As such, subtracting these PCs appeared

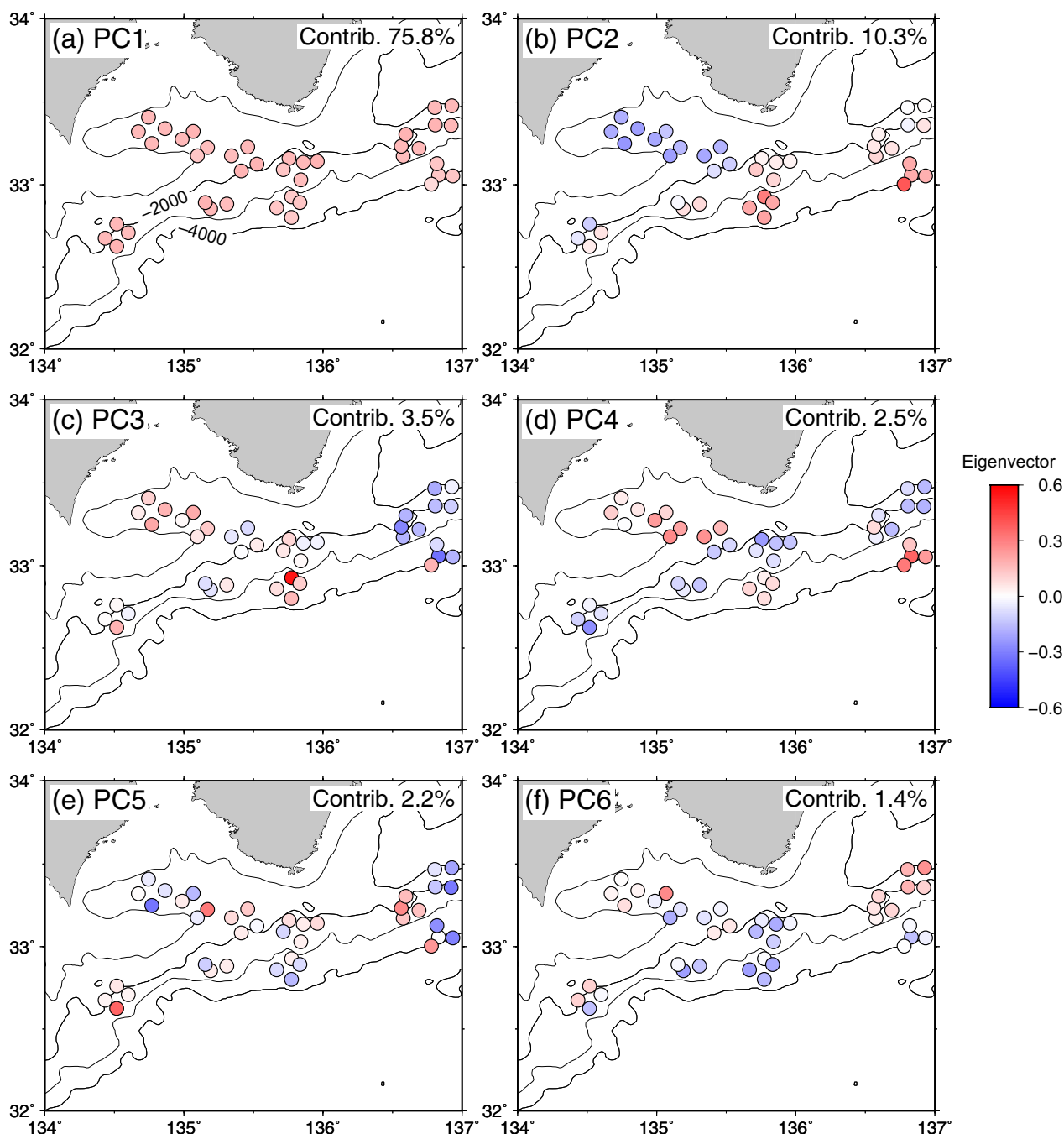


**Fig. 3** Spatial distributions for each principal component: **a** Spatial variation of the PC-1 calculated using PCA, **b** for PC-2, **c** for PC-3, **d** for PC-4, **e** for PC-5, and **f** for PC-6. The contribution of each PC is shown at the right-top of the figure

to be a reasonable procedure. In particular, PC-1 and PC-2 reflected most of the common or depth-dependent gradients of oceanographic fluctuations in the OBP time series, given that their sum contributions of both reached 86.0% and that of PC-3 and PC-4, which also reflect the oceanic signal, were only 6.0% (Fig. 4). These results

suggest that PCA can efficiently remove depth-dependent oceanographic fluctuations (Fredrickson et al. 2019; Muramoto et al. 2019; Inoue et al. 2021). In addition, reducing the noise level via pressure values at individual sites rather than calculating the pressure differences between sites is considered a significant advantage. The

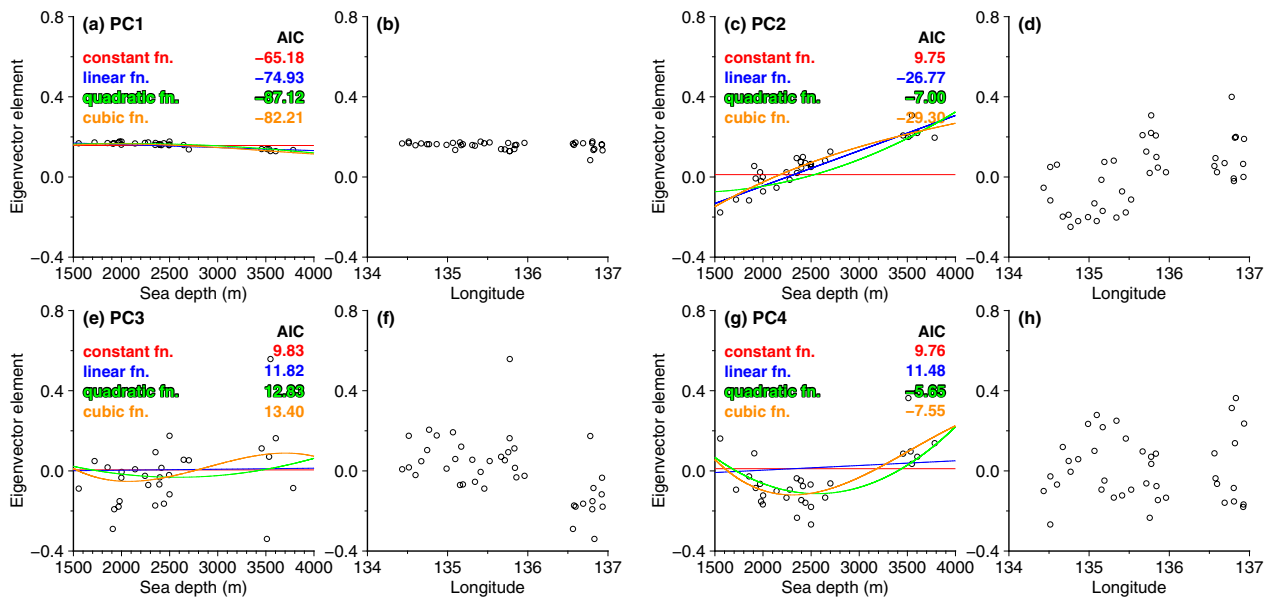


**Fig. 4** Eigenvector amplitude comparison with sea depth and longitude. The PC-1 variation along with **a** sea depth and **b** longitude. **c, d** Same as **a, b** but for PC-2. **e, f** Same as **a, b** but for PC-3. **g, h** Same as **a, b** but for PC-4. The red, blue, green, and orange lines indicate the approximations using a constant, linear, quadratic, and cubic function, respectively. The AIC (Akaike 1973) rates of each approximation are shown in the top right figure in **(a), (c), (e), and (g)**

ensuing section further confirms the details of the extent to which the PCA removes these depth-dependent oceanographic fluctuations.

### Reduction of sea-depth dependency based on PCA

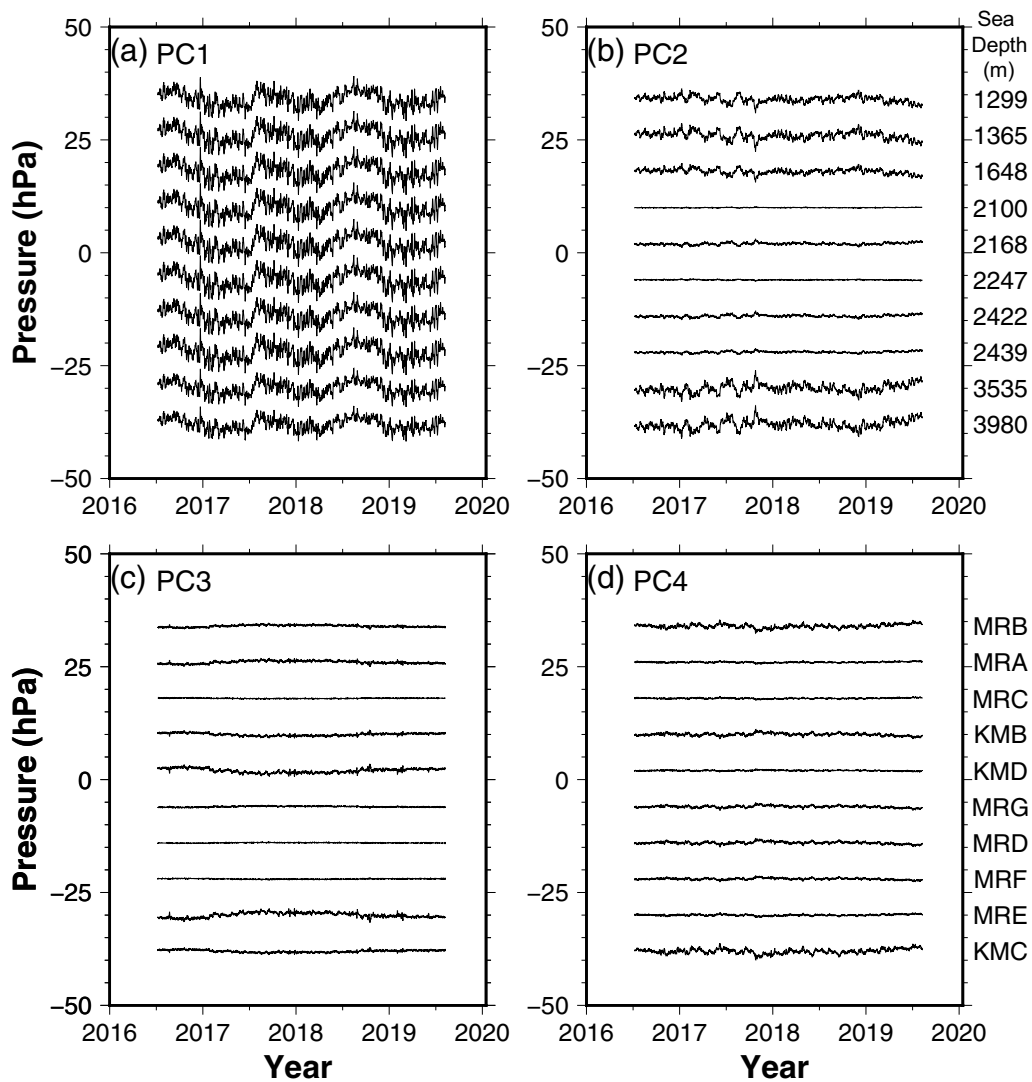
In this section, we quantitatively discuss the extent to which these depth dependencies are reduced by PCA. First, we calculated the relative pressure time series for all the stations. This was followed by calculating the RSDs and plotting them as a function of the difference in depth or distance between sites. In addition, correlation coefficients were calculated to quantitatively evaluate the dependence.

Figure 7a–b shows the sea depth and distance dependency, respectively, before PCA was applied to the time series. The results for Hikurangi, New Zealand, by Inoue et al. (2021) have also been included for comparison (Fig. 7a–b). This figure shows that the dependence on depth is greater than that on distance. This trend is also consistent with that of the off-Hikurangi margin. Figure 7c–d shows the correlation plot when PC-1 was subtracted from the original observed time series. It is interesting to note that the depth dependence visible in the original time series was not reduced. This result suggests that PC-1 contains a common component throughout the observational network, which contributes little to the spatial variation of the observed data even after its influence is removed. The results of subtracting PC-1 and PC-2 (Fig. 7e–f) indicate that

subtracting PC-2 significantly reduced the dependence on sea depth. The correlation coefficient when only PC-1 was subtracted was 0.78, which was almost halved to 0.40 when both PC-1 and PC-2 were subtracted. Interestingly, for distance dependence, the ASD itself decreased significantly (from 0.91 to 0.69), although the value of the correlation coefficient itself did not change significantly (from 0.35 to 0.30). This suggests that PC-2 can adequately remove only the sea depth-dependent component of the OBP time series. The fact that the DONET observation network has a slightly elongated shape in the direction of the isobaths (Fig. 1) also helps ensure that the removal of the sea depth dependence does not reduce the distance dependence. Figure 7i–j shows the results obtained after subtracting PCs 1, 2, and 4. Consequently, the depth dependence was further reduced with a correlation coefficient of 0.33, approximately 60% smaller than that of the original time series. However, Fig. 7g–h shows the result after subtracting PCs 1–3. PC-3 does not reduce the sea depth dependence (from 0.40 to 0.40), although it slightly reduces the distance dependence (from 0.30 to 0.26). After removing PCs 1, 2, and 4 or PCs 1–4, the correlation coefficient of the sea-depth dependence is almost equivalent to the distance dependence, indicating that removing PCs 1, 2, and 4 can significantly reduce the depth dependence of oceanographic fluctuations (Fig. 7k–l).

Previous studies have noted that applying PCA may reduce the detection accuracy of crustal deformation





**Fig. 5** Principal component time series for each node. Each principal component time series sorted by sea depth. The time series for **a** PC-1, **b** PC-2, **c** PC-3, and **d** PC-4. The rough sea depths and the station names are shown on the right side of **(a)** and **(d)**, respectively. The time series for each station are referenced in Additional file 1: Fig. S13

owing to the seepage of crustal deformation components into the PCs (Watts et al. 2021; Fredrickson et al. 2023). Therefore, in the next section, we discuss the accuracy of crustal deformation detection by PCA using synthetic rectangular faults in the observation region.

**Physical oceanographic interpretation of each principal component**

In the previous section, PCA was used to successfully extract components with multiple spatial characteristics. The observed pressure time series includes both oceanographic fluctuations and tectonic signals; however, the oceanographic circulation models include only

the oceanographic fluctuations. To examine the characteristics of oceanographic fluctuations, we applied PCA to ocean models and compared the spatial distribution of each PC with the observation. The ocean models have advantages and disadvantages in the region and time scale used herein, depending on the input data and model structure (Dobashi and Inazu 2021). We chose a single-layer ocean model (SOM) (Inazu et al. 2012) and ECCO2 (Menemenlis et al. 2008) for comparison with observations. SOM assumes a single-layer barotropic ocean model and is driven by atmospheric pressure as well as wind stress, whereas ECCO2 assumes a multiple-layer (50 layers) baroclinic ocean model (that is, better vertical resolution than SOM) and is driven by wind

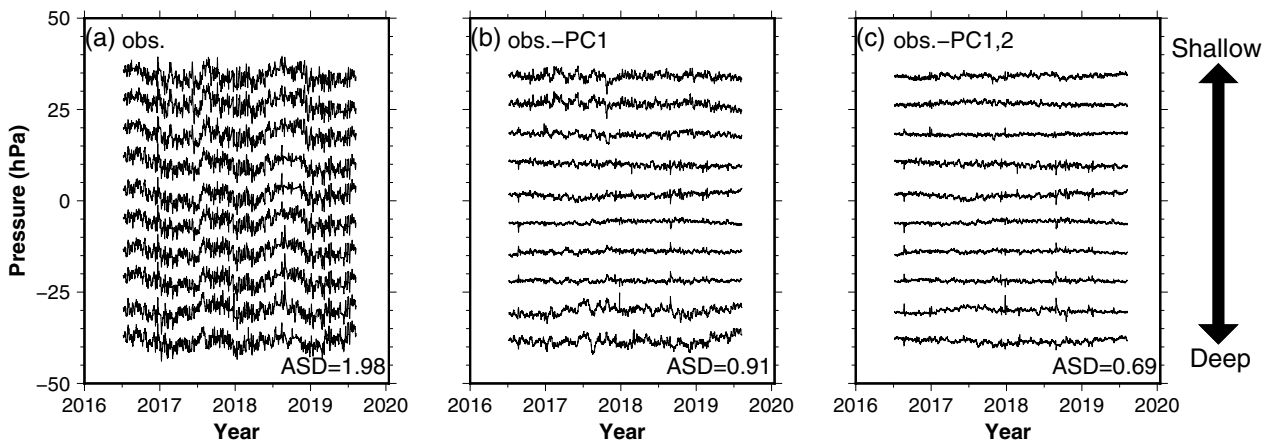


**Fig. 6** OBP time series for each node with offset sorted by sea depth: (a) the observations, (b) after removing PC-1, and (c) after removing PC-1 and PC-2. The averaged standard deviation (ASD) of each process is (a) 1.98, (b) 0.91, and (c) 0.69. The beards in the time series are caused by the interpolation of the missing period. The time series for each station are referenced in Additional file 1: Fig. S14

stress, heat, and freshwater flux, although the atmospheric pressure is not considered. The details of each model are listed in Table 2 by Dobashi and Inazu (2021). The expected pressure time series was calculated based on each model. As each numerical model provides calculations for each grid, the grid nearest to the DONET observation region (77 grids in longitude of 134°E–137°E and latitude of 32°N–34°N) was selected, and PCA was applied to the time series data to confirm the characteristics of the model.

After applying PCA to SOM, the PC-1 contribution reached 96.7% (Additional file 1: Fig. S3a). This is clearly larger than the 75.7% observed (Fig. 3), indicating that ocean variations show similar fluctuations (Additional file 1: Fig. S3). Overall, the oceanographic fluctuations expressed pressure variations, but their contribution was more exaggerated than the observation. In contrast, higher-order terms, such as the sea depth-dependent component identified in the observational data, were poorly extracted from the SOM. Importantly, when applying PCA to ECCO2, PC-1, PC-2, PC-3, and PC-4 contributed 80.8%, 9.9%, 2.9%, and 1.8%, respectively. The contribution ratio and the spatial distribution (Additional file 1: Fig. S6) were similar to the observational data (Fig. 3). The reproduced oceanographic fluctuations calculated by ECCO2 are more realistic than SOM.

The extracted PC characteristics of ECCO2 were as follows. PC-1 was the overall pressure variation with a large spatial scale (several hundred km extent) driven by wind stress and atmospheric pressure, which was also reproduced by SOM. PC-2 was the depth-dependent component (a pattern orthogonal to isobath). PC-3 and PC-4 were the depth-dependent patterns, but their frequency was higher than PC-2 (Additional file 1: Figs. S6 and S8). The longitudinal dependence component seen in PC-3 or PC-4 of ECCO2 and is considered to be included in these components.

Following confirmation that the PCs extracted from the observed time series were due to oceanographic fluctuations, we attempted to interpret them qualitatively. The Nankai Trough, where DONET stations are installed, is a channel of the Kuroshio current (e.g., Nitani 1972), which meanders widely on time scales of several years or more (e.g., Kawabe 1985). For example, one of the largest Kuroshio meanders occurred in 2017 and continued through 2022, contributing to pressure fluctuations on the seafloor (Nagano et al. 2019; 2021). Therefore, oceanographic phenomena such as the strength and meandering of the Kuroshio current should be recorded in the OBP data for the DONET region. The meandering of the geostrophic current including Kuroshio is interrelated with the mesoscale eddy (Qiu and Miao 2000; Hasegawa et al.

(See figure on next page.)

**Fig. 7** Time series variation of each observation point as a function of sea depth and distance. The correlation distribution between the standard deviation of the relative pressure time series and the station distance **a, c, e, g, i, k** or the sea-depth difference **b, d, f, h, j, l**. The standard deviation is calculated for (a, b) the observation, (c, d) after removing PC-1, (e, f) after removing PC-1 and PC-2, (g, h) after removing PCs 1–3, (i, j) after removing PCs 1, 2, and 4, and (k, l) after removing PCs 1–4. Black dots indicate the correlation between the standard deviation and the distance or the sea depth for each relative pressure time series. Red dots indicate the same thing as the black dots but for the off-Hikurangi margin (Inoue et al. 2021). The upper number is the correlation coefficient between the two axes for each figure

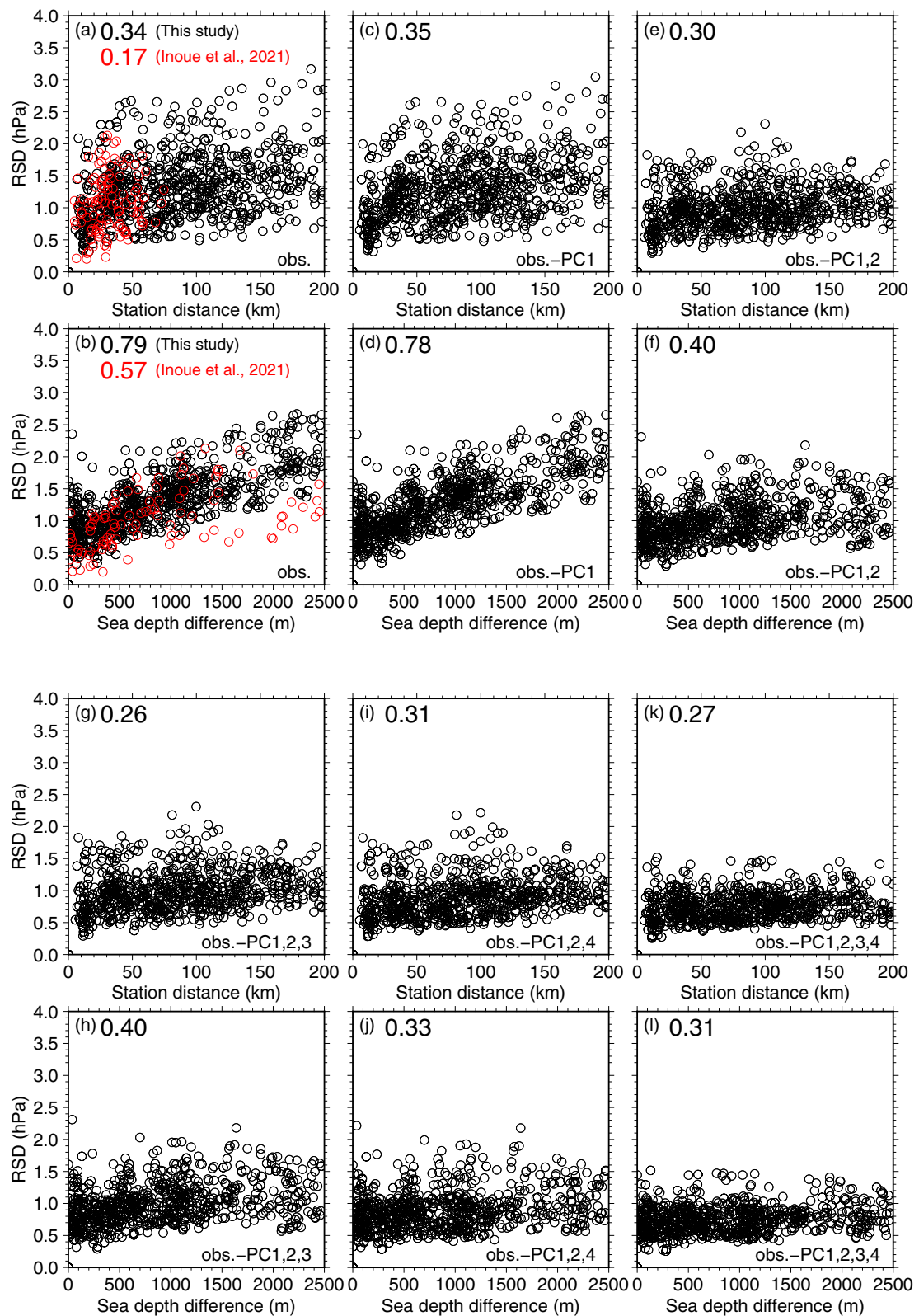


**Fig. 7** (See legend on previous page.)

2019) at approximately 100 km radius and their contribution to the sea bottom pressure perturbation cannot be well separated. Note that the sea level variation due to the meso-scale eddies is considerably attenuated to the ocean-bottom pressure variation because the sub-sea surface water column imperfectly compensates for the pressure change by sea surface variation (Dobashi and Inazu 2021; Hasegawa et al. 2021).

Based on the results of the application of PCA to the observed data and ocean models, and the previous studies on oceanographic fluctuations and the Kuroshio current (Hasegawa et al. 2021), each PC in the observed data was interpreted as follows. PC-1 is the large spatial scale variation associated with wind stress and atmospheric pressure variation. PC-2 corresponds to the strength and weakness, and flow axis position of the geostrophic current (that is, Kuroshio current) (Fig. 8a). Both PC-3 and PC-4 might be compatible with the spatial pattern depending on the location of the mesoscale eddy, which has a radius of fewer than 50 km (Fig. 8b–c). If the centroid of the cold vortex is located east (Fig. 8b) or west (Fig. 8c) of the Kii Peninsula, the longitudinal dependence variation might be reflected in the observed DONET data. A parabola-like spatial distribution can occur when the cold vortex migrates eastward or westward, orthogonal to the direction of the isobath (that is, changes from Fig. 8b to c or Fig. 8c to b). In our analysis, it was not necessarily possible to distinguish whether the cold vortex was located east (Fig. 8b) or west (Fig. 8c) of the Kii Peninsula, however, we inferred that it has a spatial distribution that reflects these oceanophysical phenomena in PCs 3 and 4. As mentioned above, the sea-surface level fluctuations are not directly reflected as seafloor pressure variations, but fluctuations caused by mesoscale eddies are thought to affect ocean bottom pressure.

In these analyses, PCA was applied to a long-term continuous time series of more than 3 years. However, if the components reflected in the PCs have characteristic time constants, changing the time window may change the extracted components. Nevertheless, applying PCA to the OBP time series shows that pressure fluctuations of oceanic origin can be separated based on their spatial characteristics. This suggests that the method can improve the quality of time series data when extracting pressure variations caused by crustal deformation. In the following section, we discuss the potential usefulness of PCA when transient crustal deformations are included in a time series.

#### Synthetic test for principal component analysis to observe crustal deformation

Discussions so far suggest that applying PCA to the DONET time series can separate the non-tidal

oceanographic fluctuations in the observed data; PC-2 and PC-4 could explain the most depth-dependent oceanographic fluctuations in the OBP time series. In contrast, it is necessary to evaluate the ability of PCA to separate transient tectonic and oceanographic signals to improve the reliability of crustal deformation observations using OBPs. Watts et al. (2021) performed a complex PCA after adding a synthetic ramp function to the OBP time series of four stations and found that part of the ramp signal interfered with the principal component, which mainly reflects oceanographic fluctuations. This result suggests that subtracting the oceanographic component from the observed time series also removes part of the tectonic signal and may underestimate the displacement amplitude caused by the transient event. This section evaluates the possibility of separating tectonic and oceanographic signals by applying PCA to the OBP time series. In this analysis, we assumed that the tectonic signals of SSE detected by several previous studies (e.g., Araki et al. 2017; Ariyoshi et al. 2021) did not accompany sufficient amplitude to detect the OBP of the seafloor vertical displacement.

#### Analytical overview of the synthetic test

This section describes a method to add a synthetic signal to the OBP time series using a rectangular fault model (Okada 1992). The results were assumed for each earthquake moment magnitude ( $M_W$  5.5–7.0, 0.1 increments) based on the scaling law proposed by Wells and Coppersmith (1994). The rigidity and Poisson's ratio were set for 30 GPa and 0.25, respectively. The faults were located along the plate boundary of the Philippine Sea Plate (Baba et al. 2002; Hirose et al. 2008; Iwasaki et al. 2015). The strike, dip, and rake angles of the fault used were 250°, 8°, and 90°, respectively, assuming a reverse fault along the plate boundary. The assumed fault model was horizontally spaced at 0.1° intervals. Additional file 1: Figure S9 shows the centroid of all 548 fault planes. For each assumed fault model, the time evolution of the fault slip was calculated using a ramp function based on the duration and total amount of slip expected from the moment magnitude. The duration of an SSE was estimated using Eq. 4, following the scaling law between the magnitude and duration estimated by the observed slow earthquakes (Ide et al. 2007):

$$Mo \sim T \times 10^{12-13} \quad (4)$$

where  $Mo$  indicates the seismic moment [N m] and  $T$  indicates the duration period [s]. In this study, we calculated the value of the duration  $T$  using the observed SSE parameter around the Kii Peninsula investigated by Sekine et al. (2010), which is as follows:

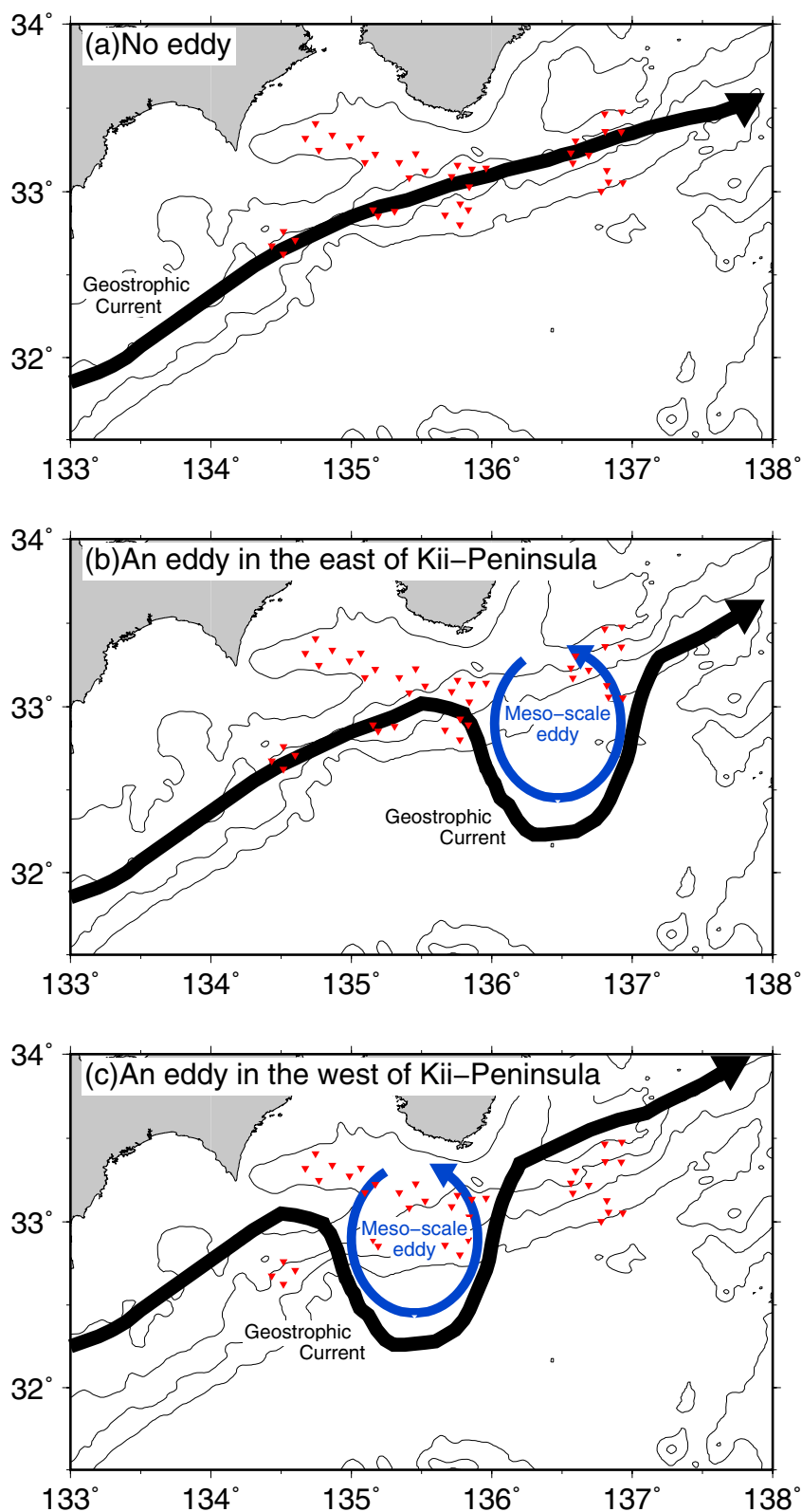


**Fig. 8** Sketches on the interpretation of the spatial distribution of each principal component. **a** The geostrophic current (Kuroshio current) without meandering and eddy. **b, c** The geostrophic current with a mesoscale eddy (cold vortex) located in the southeast/west of the Kii Peninsula. The bold black arrow indicates the flow path of the geostrophic current. The blue arrow indicates the image of the mesoscale eddy corresponding to the geostrophic current. Red triangles indicate the DONET observation points used in this study

$$M_o = T \times 10^{12.2} \quad (5)$$

Table 1 shows the duration and length of the rectangular faults as well as other parameters at representative magnitudes calculated based on the results of Wells and Coppersmith (1994) and Eq. 5. The timing of the synthetic ramp application was set so that the center of the lamp coincided with the middle of the entire observation period (January 1st, 2018).

#### Extraction of transient crustal deformation by PCA

A ramp function with an amplitude duration corresponding to the fault position and earthquake size was added to the observed OBP time series. PCA was applied to investigate how the components that responded to the ramp function were affected by the PCs. The OBP time series expected by the  $M_W$  7.0 event at 135.5°E and 33.0°N has been shown in Fig. 9a, and the spatial distribution of sea-floor vertical displacement and each PC in Fig. 10b–f. In this case, the vertical displacement at the station reached a 20.1 cm uplift (20.1 hPa pressure decrease) at station MRE21 (Fig. 9b). The vertical displacement associated with SSE was extracted as PC-1. The common, depth, and longitude-dependent components were extracted from PCs 2, 3, 4, and 5, respectively (Fig. 10c–f). In contrast, when the  $M_W$  6.7 event at the same location fault was assumed, a PC including the assumed ramp function was classified into PCs 1 and 2 (Fig. 10b–c). PCs 1 and 2 also included the common components, while PCs 3–5 included depth-dependent and longitude-dependent components (Fig. 10d–f). The assumed ramp and common components were mixed in PCs 1 and 2 because of their similar amplitude; the contributions of PC-1 and PC-2 were 53.1% and 35.6%, respectively. This result indicates that each PC was shifted to higher-order modes by one before displacement by the SSE was added. In this example, the expected displacements were sufficiently large compared to the accuracy of the OBP observations, which were classified as PC-1. Figure 11 illustrates

the PCs extracted for each component as the earthquake magnitude was reduced for the same fault location. From this figure, it can be observed that the displacement field expected by the SSE gradually shifts to a higher-order mode.

These results suggest that PCA can be applied to the time series of transient crustal deformations caused by SSE to extract those tectonic signals as PCs along with oceanographic fluctuations. Thus, the PCs of the time series include transient crustal deformation and those that do not include the deformation can be compared; in other words, if the difference between their spatial distributions (each eigenvector element) is significant, they can be extracted. In subsequent sections, we propose a method for evaluating crustal deformation using the spatial distribution of PCs estimated by PCA and evaluate its effectiveness.

#### Evaluation of spatial characteristics between the PCs

We used the absolute value of the normalized inner product (NIP) of the eigenvectors to estimate the spatial characteristics of the results extracted using PCA. The amplitude of each OBP site for each PC corresponded to each element of the eigenvector PC. The NIP of two eigenvectors of the same value was found to be 1; if the difference between them was large, the value was close to 0. When the amplitude of the OBP time series due to crustal deformation is smaller, crustal deformation signals and oceanographic fluctuations may be mixed in the same PC. Additional file 1: Figure S10 shows the spatial distribution of PC-2 for each magnitude, assuming a rectangular fault at 135.5°E, 33.0°N. This shows that if the event is small and the expected crustal deformation is classified as PC-1 and/or PC-2, then PC-2 includes other noise components like oceanographic fluctuations. Therefore, in this section, we consider using the PC-2 difference, with and without synthetic crustal deformation to improve the efficiency of crustal deformation detectors using PCA. Table 2 shows the NIP between the

**Table 1** Duration, length, and slip of rectangular fault calculated for each moment magnitude (Wells and Coppersmith 1994) (Eq. 3)

$M_W$	Duration (days)	Length (km)	Slip (cm)	$M_W$	Duration (days)	Length (km)	Slip (cm)
5.5	1.6	5.9	28.7	6.3	25.9	17.1	73.4
5.6	2.3	6.7	32.3	6.4	36.6	19.6	82.6
5.7	3.3	7.7	36.3	6.5	51.7	22.4	92.9
5.8	4.6	8.8	40.8	6.6	73.0	25.6	104.4
5.9	6.5	10.0	45.9	6.7	103.2	29.2	117.5
6.0	9.2	11.5	51.6	6.8	145.7	33.4	132.1
6.1	13.0	13.1	58.1	6.9	205.8	38.2	148.6
6.2	18.3	15.0	65.3	7.0	290.7	43.7	167.1

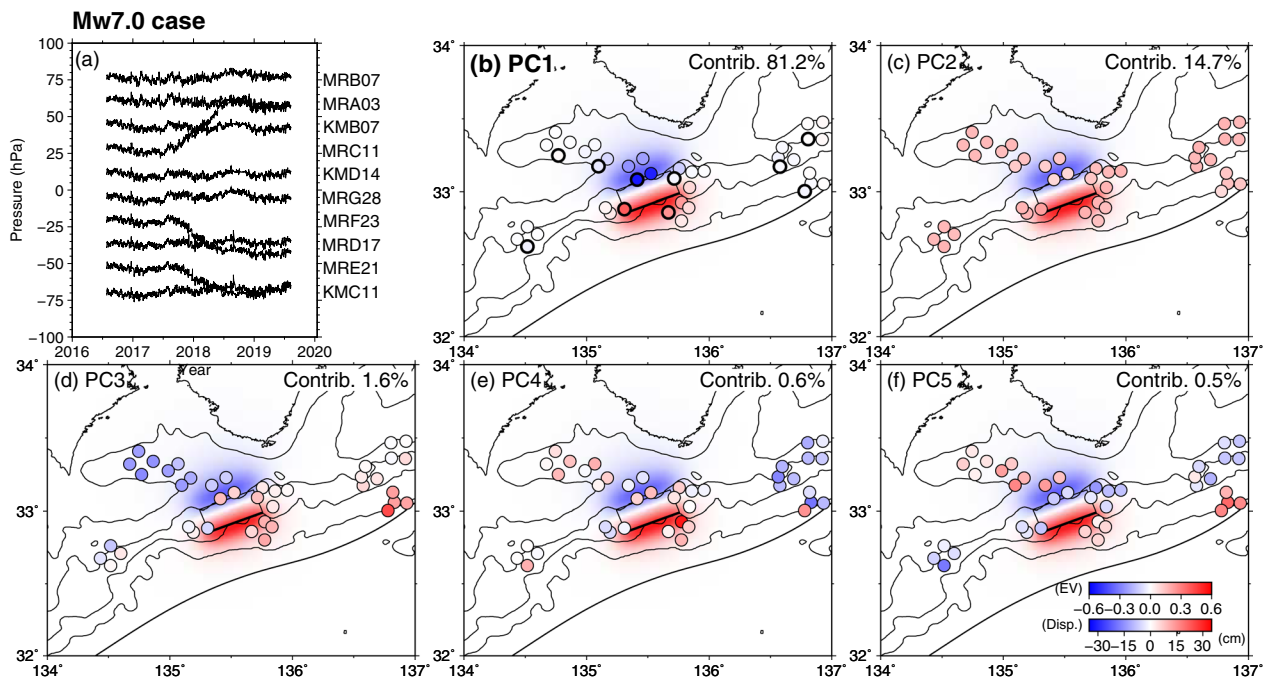


**Fig. 9** Time series and spatial distribution of PC assuming a synthetic fault model of  $M_w$  7.0. The center of the fault was at  $135.5^\circ\text{E}$ ,  $33.0^\circ\text{N}$ . Figures with bold captions reflect the assumed synthetic ramp (here, **(b)** reflects the synthetic ramp). **a** The pressure time series represents each node after applying a synthetic ramp to the observed time series (Fig. 6a). **b** Spatial distribution of the PC-1 when PCA is applied to the time series in **(a)**. The bold circles indicate the observation sites whose time series are illustrated in **(a)**. **c–f** Same as **b**, but for PC-2, PC-3, PC-4, and PC-5, respectively. The rectangular area indicates the assumed fault model and the background color shows the vertical displacement calculated from the synthetic fault model. The thin line indicates the isobath with an interval of 1000 m

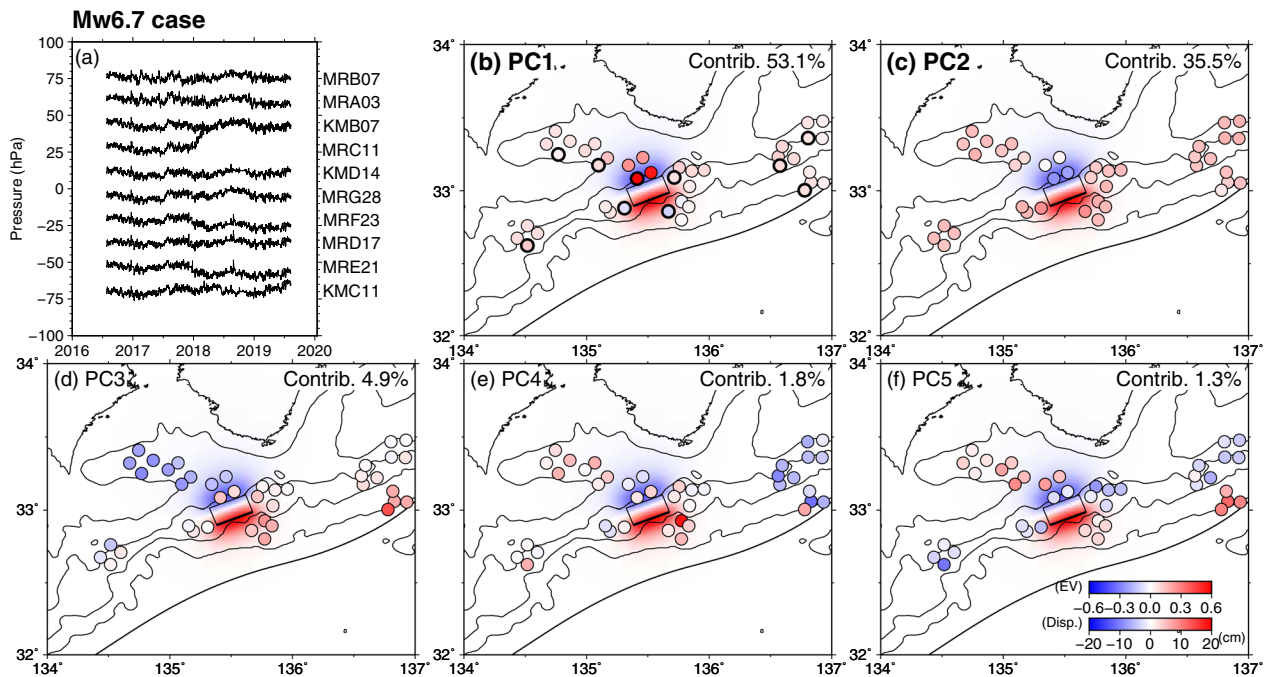


**Fig. 10** Time series **(a)** and spatial distribution **(b–f)** of PC assuming a synthetic fault model of  $M_w$  6.7. In this case, **b** and **c** reflect the synthetic ramp

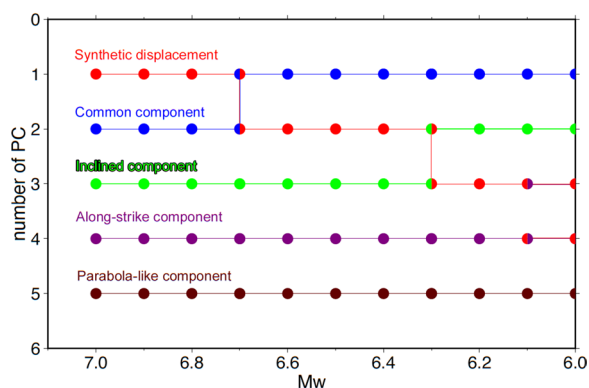


**Fig. 11** PC variation per  $M_w$  for a fault center of 135.5°E, 33.0°N. The interpretation of each PC was based on their spatial distributions. As the  $M_w$  decreases, the applied synthetic displacement component migrates to higher-order PCs. In the  $M_w$  6.7 and  $M_w$  6.3 cases, the spatial distribution characteristics of PC-1 and PC-2 or PC-2 and PC-3, respectively, are mixed

**Table 2** NIP between the two PC-2 s for each moment magnitude, assuming a rectangular fault at 135.5°E, 33.0°N. The spatial distribution of each PC-2 is shown in Additional file 1: Fig. S11

$M_w$	NIP
5.5	1.00
5.6	1.00
5.7	1.00
5.8	1.00
5.9	1.00
6.0	1.00
6.1	1.00
6.2	0.99
6.3	0.78
6.4	0.40
6.5	0.32
6.6	0.30
6.7	0.21
6.8	0.12
6.9	0.09
7.0	0.07

two PC-2 s without changing the fault location. In this example, if the assumed event were a fault with a magnitude of  $M_w$  6.2 or less, the crustal deformation component would be classified as PC-3, in which case the NIP would be approximately 1. In other cases, the expected crustal deformation components are not separated into independent PCs but mixed with other oceanographic fluctuations ( $M_w$  6.7 and  $M_w$  6.3 in Fig. 11). For example, for  $M_w$  6.3, the NIP of PC-2 was 0.78, and its spatial

distribution included inclined oceanographic fluctuations and crustal deformation (Additional file 1: Fig. S10).

**Comprehensive synthetic test for PCA**

Based on the evaluation of spatial characteristics of the results of PCA, we conducted analyses (assuming faults) using NIP as a proxy for each grid assuming faults and quantitatively evaluated the magnitude of events detected by PCA. Additional file 1: Figure S11 shows the results when 0.99, 0.90, ... 0.01 was used as the upper NIP limit threshold between PC-2 s (that is, a change was detected when  $NIP < 0.99$ ,  $NIP < 0.90$ , 0.01). The ability to detect crustal deformation is naturally higher in the neighborhood of OBP sites, and the magnitude of the moment of the lower detection limit increases with distance. On the onshore side—away from the trench axis—the plate boundary is relatively deeper, and the expected displacement is smaller; therefore, the lower detection limit for the magnitude is larger. Alternatively, land-side crustal deformations can be observed using on-land continuous Global Navigation Satellite System (GNSS) sites (e.g., GEONET; GNSS Earth Observation Network System operated by the Geospatial Information Authority of Japan [GSI]). In addition, the  $M_w$  6–6.5 events could be detected by only on-land GNSS (Suito 2016). The accuracy of SSE detection was also examined by integrating both on-land and seafloor observation networks (Agata et al. 2019); however, this is beyond the scope of this study.

The lower limit of the event size at which crustal deformation can be strongly detected depends on the NIP threshold. Naturally, the threshold value is smaller, and the lower limit of the detectable  $M_w$  is larger (Additional file 1: Fig. S11). To determine the best NIP threshold for these analyses, we focused on the NIP variation depending on the  $M_w$  migration. The NIP changed with the  $M_w$  for each rectangular fault point; the maximum NIP change at 135.5°E, 33.0°N was 0.38 (from 0.40 to 0.78) during the  $M_w$  migration between 6.4 and 6.3 (Additional file 1: Fig. S10). Similarly, a comparison of the pattern of change in  $M_w$  and NIP for each rectangular fault showed that NIP changed abruptly at each specific  $M_w$ . This suggests that the crustal deformation component clearly migrates to higher-order modes as  $M_w$  is reduced for almost all fault locations (Additional file 1: Fig. S11). We fixed every NIP change pattern by the largest change in NIP and examined the average and SD at each  $M_w$  (Additional file 1: Fig. S12). In Additional file 1: Fig. S12, the largest NIP change was set as the relative  $M_w$  between 0.1 and 0.0. The NIPs above 1σ, at the lower and upper side of the largest NIP change were between 0.52 and 0.75. Consequently, we propose that a practical NIP threshold value be included in this range. In comparing



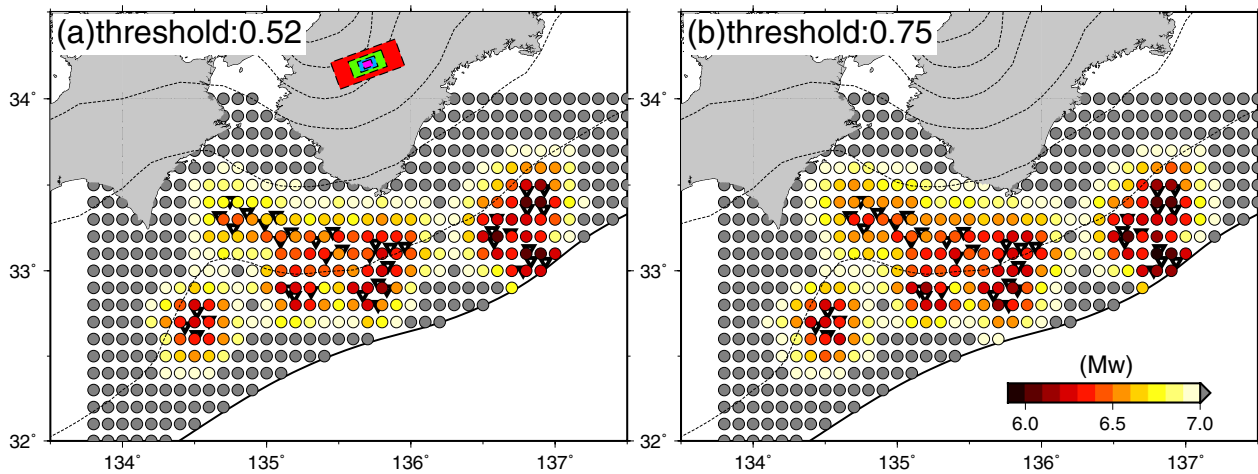


**Fig. 12** Spatial distributions of  $M_W$  at the lower limit of event detection. **a** The lower limit of the detectable  $M_W$  for each center position of the synthetic rectangular fault using only OBP data and PCA for the threshold of 0.52. **b** Same as **(a)**, but for the threshold of 0.75. The rectangles with dotted lines indicate the case of  $M_W$  7.0 (red),  $M_W$  6.5 (green),  $M_W$  6.0 (light blue), and  $M_W$  5.5 (pink). The dashed lines indicate the depth of the plate boundary with an interval of 10 km (Baba et al. 2002; Hirose et al. 2008; Iwasaki et al. 2015)

the cases with NIP thresholds of 0.52 and 0.75, the lower detection limit  $M_W$  was naturally smaller for 0.75, whereas the overall spatial distribution was generally consistent (Fig. 12). This suggests that the anomaly detection ability of our method is not significantly different when the threshold value is selected within this range. In the case of a NIP threshold value of 0.75, at the rectangular fault at 136.8°E, 33.1°N, the smallest event of  $M_W$  5.9 can be detected by our detection method (Fig. 12). The spatial distribution of the lower limit of the moment magnitude of a detectable event corresponds to a pressure step with an amplitude greater than one signal-to-noise ratio at five or more stations. The reason the fault at this location was on the lower limit of detection is thought to be because the assumed fault depth was relatively shallow and located near the observation point.

## Conclusions

By applying PCA to the DONET OBP time series from 2016 to 2019, we verified the spatiotemporal characteristics of oceanographic fluctuations in the Nankai region of Japan. The oceanographic fluctuation characteristics of sea-depth dependency found by Inoue et al. (2021) were verified in the Nankai region and were reflected in PC-2 and PC-4. From the spatial distribution of these PCs, we inferred that these sea-depth dependencies were caused by the strength and the meandering of ocean geostrophic currents and mesoscale eddies. Finally, we could not detect significant transient tectonic events in the OBP time series, suggesting that the amplitude of the transient events was too small to be detected, or the signal seeped into the PCs interpreted as oceanographic fluctuations.

We added synthetic ramps, assuming an SSE of moment magnitude between 5.5 and 7.0, to the observed time series to evaluate the ability of PCA to separate tectonic and oceanic signals. The added synthetic ramp signal can be divided into independent PCs depending on their scale. We proposed a transient event-detection method using PCA applied to the OBP time series. The lower limit of the magnitude of the detectable event depends on the NIP threshold, although the  $M_W$  5.9 event can be detected from the pressure data on the rectangular fault with the best observation points. Although we assumed that the observed OBP data do not contain detectable transient tectonic signals, in the future, we intend to systematically detect SSEs using this method and compare them with slow earthquake activity detected previously to better understand the occurrence mechanisms of slow earthquakes.

## Abbreviations

ASD	Averaged standard deviation
BAYTAP-G	Bayesian Tidal Analysis Program-Grouping Model program
DONET	Dense Oceanfloor Network System for Earthquakes and Tsunamis
ECCO	Estimating the Circulation and Climate of the Ocean
GEONET	GNSS Earth Observation Network System
GNSS	Global Navigation Satellite System
GSI	Geospatial Information Authority of Japan
HOBITSS	Hikurangi Ocean Bottom Investigation of Tremor and Slow Slip
JAMSTEC	Japan Agency for Marine-Earth Science and Technology
$M_W$	Moment magnitude
NIED	National Research Institute for Earth Science and Disaster Resilience
NIP	Normalized inner product
OBP	Ocean bottom pressure-gauge
PC	Principal component
PCA	Principal component analysis
RSD	Relative standard deviation

SD Standard deviation  
 SOM Single-layer ocean model  
 SSE Slow slip event

## Supplementary Information

The online version contains supplementary material available at <https://doi.org/10.1186/s40623-023-01862-z>.

**Additional file 1: Figure S1.** Observed time series sorted by station number. Each time series is color-coded by the observation node, and the node name and average correlation coefficient within the node are shown in the same color as the time series on the right. **Figure S2.** OBP time series with offset sorted by sea depth after removing PCs 1 and 2 from (a) the observations (Same figures as Figure 6(c)), (b) after removing PCs 1–3, (c) after removing PCs 1, 2 and 4, and (d) after removing PCs 1–4. The averaged standard deviation (ASD) of each process is (a) 0.69, (b) 0.61, (c) 0.62, and (d) 0.53. **Figure S3.** (a) Spatial distribution of the PC-1 for SOM calculated using PCA. (b) Same as (a), but for PC-2. (c) Same as (a), but for PC-3. (d) Same as (a), but for PC-4. The time series indicate the eigenscores of each PC. **Figure S4.** (a) Time series of PC-1 for SOM. (b) Same as (a), but for PC-2. (c) Same as (a), but for PC-3. (d) Same as (a), but for PC-4. **Figure S5.** PC-1 variation along with (a) sea depth or (b) longitude for the SOM. (c, d) Same as (a, b) but for PC-2. (e, f) Same as (a, b) but for PC-3. (g, h) Same as (a, b) but for PC-4. **Figure S6.** (a) Spatial distribution of the PC 1 for ECCO2 calculated by PCA. (b) Same as (a), but for PC-2. (c) Same as (a), but for PC-3. (d) Same as (a), but for PC-4. The time series indicate the eigenscores of each PC. **Figure S7.** (a) Time series of PC-1 for ECCO2. (b) Same as (a), but for PC-2. (c) Same as (a), but for PC-3. (d) Same as (a), but for PC-4. **Figure S8.** PC-1 variation along with (a) sea depth or (b) longitude for the ECCO2. (c, d) Same as (a, b) but for PC-2. (e, f) Same as (a, b) but for PC-3. (g, h) Same as (a, b) but for PC-4. **Figure S9.** Centroid of the rectangular fault models used for the synthetic analysis test. We used the rectangular faults, whose centroids were included in the bold black line. The color indicates the plate boundary depth. **Figure S10.** Vertical displacement distributions and PC-2 spatial distribution for  $M_w$  5.9–7.0. The top right number of each figure indicates the NIP number between two PC 2s. **Figure S11.** Spatial distribution of the lower limit of synthetic ramp detection in the case of the threshold of (a) 0.99, (b) 0.90, (c) 0.80, (d) 0.70, (e) 0.60, (f) 0.50, (g) 0.40, (h) 0.30, (i) 0.20, (j) 0.10, (k) 0.05, and (l) 0.01. The detectability change corresponds to the threshold of the inner product. **Figure S12.** Every fixed NIP variation pattern for relative  $M_w$ . The gray lines indicate the NIP pattern of each rectangular fault grid for relative moment magnitude. The red point is the average of the NIP for each relative  $M_w$ . The horizontal and vertical error bars indicate the standard deviation of  $M_w$ , displacement width and NIP for each relative  $M_w$ , respectively. The horizontal dotted lines indicate the lower and upper limits of the NIP value that may be used as the threshold of detectability (Figure 12). **Figure S13.** Each principal component time series sorted by sea depth. The time series for (a) PC-1, (b) PC-2, (c) PC-3, and (d) PC-4. The rough sea depths and the station names are shown on the right side of (a) and (d), respectively. **Figure S14.** OBP time series with offset sorted by sea depth for (a) the observations, (b) after removing PC-1, and (c) after removing PC-1 and PC-2. The averaged standard deviation (ASD): (a) 1.98, (b) 0.91, and (c) 0.69. The station names are shown on the right side of the figure. The beads in the time series are caused by the interpolation of the missing period.

## Acknowledgements

We would like to thank the anonymous reviewers and the editor for their constructive comments on the manuscript. This study was supported by the Japan Science and Technology Agency (JST) Fusion Oriented Research for Disruptive Science and Technology (FOREST) Program (grant number: JPM-JFR202P, Japan). This study was also supported by the Ministry of Education, Culture, Sport, Science and Technology (MEXT) of Japan under The Second Earthquake and Volcano Hazards Observation and Research Program (Earthquake and Volcano Hazard Reduction Research). This work was also supported by the Research Project for Disaster Prevention on the Great Earthquakes along the Nankai Trough by MEXT. WISE Program for Sustainability in the

Dynamic Earth supported Hideto Otsuka financially. All figures in this paper were created by Generic Mapping Tools 5 (Wessel et al. 2013). We would like to thank Editage ([www.editage.com](http://www.editage.com)) for English language editing.

## Author contributions

HO, YO, and RH designed this study. HO analyzed the data, prepared figures, and drafted the manuscript. HO, YO, RH, TK, DI, and TI helped with data interpretation. TK and NT retrieved the DONET observed data from National Research Institute for Earth Science and Disaster Resilience (NIED) and Japan Agency for Marine-Earth Science and Technology (JAMSTEC). Every author read and approved the final manuscript.

## Funding

This study was supported by the Japan Science and Technology Agency (JST) Fusion Oriented Research for Disruptive Science and Technology (FOREST) Program (grant number: JPMJFR202P, Japan). This study was also supported by the Ministry of Education, Culture, Sport, Science and Technology (MEXT) of Japan under The Second Earthquake and Volcano Hazards Observation and Research Program (Earthquake and Volcano Hazard Reduction Research). This work was also supported by the Research Project for Disaster Prevention on the Great Earthquakes along the Nankai Trough by MEXT.

## Availability of data and materials

The DONET (<https://doi.org/10.17596/0002216>, <https://doi.org/10.17596/NIED.0008>) is jointly operated by the Japan Agency for Marine-Earth Science and Technology (JAMSTEC) and the National Research Institute for Earth Science and Disaster Resilience (NIED) after April 1st, 2016, and the seafloor pressure data during this period is available with data request and permission at the website of NIED (<https://hinetwww11.bosai.go.jp/auth/oc/>, accessed on November 1st, 2022). DONET was operated by JAMSTEC before March 31st, 2016, and the data in this period is available at the website of JAMSTEC ([https://www.jamstec.go.jp/ceat/donet\\_data/j/technical/](https://www.jamstec.go.jp/ceat/donet_data/j/technical/) and <https://join-web.jamstec.go.jp/join-portal/>, accessed in 2018). The data access is currently partially suspended and inquiries are needed ([https://www.jamstec.go.jp/e/about/informations/notification\\_2021\\_maintenance.html](https://www.jamstec.go.jp/e/about/informations/notification_2021_maintenance.html), accessed on November 1st, 2022).

## Declarations

### Ethics approval and consent to participate

Not applicable

### Consent for publication

Not applicable

### Competing interests

The authors declare that they have no competing interests.

## Author details

<sup>1</sup>Graduate School of Science, Tohoku University, 6-6 Aramaki-Aza-Aoba, Aoba-Ku, Sendai, Miyagi 980-8578, Japan. <sup>2</sup>National Research Institute for Earth Science and Disaster Resilience, 3-1 Tennodai, Tsukuba, Ibaraki 305-0006, Japan. <sup>3</sup>Department of Marine Resources and Energy, Tokyo University of Marine Science and Technology, 4-5-7 Konan, Minato-Ku, Tokyo 108-8477, Japan. <sup>4</sup>Graduate School of Science, Kyoto University, Kitashirakawa-Oiwake, Sakyo-Ku, Kyoto 606-8502, Japan. <sup>5</sup>Institute of Industrial Science, The University of Tokyo, 4-6-1 Komaba, Meguro-Ku, Tokyo 153-8505, Japan. <sup>6</sup>Japan Agency for Marine-Earth Science and Technology, 3173-25 Showa, Kanazawa-Ku, Yokohama, Kanagawa 236-0001, Japan.

Received: 19 February 2023 Accepted: 26 June 2023

Published online: 18 July 2023

## References

Agata R, Hori T, Ariyoshi K, Ichimura T (2019) Detectability analysis of interplate fault slips in the Nankai subduction thrust using seafloor observation instruments. *Mar Geophys Res* 40:453–466. <https://doi.org/10.1007/s11001-019-09380-y>

- Akaike H (1973) Information theory and an extension of the maximum likelihood principle. In: Petrov BN, Caski F (eds) 2nd International Symposium on Information Theory. Akademiai Kiado, Budapest
- Androsov A, Boebel O, Schröter J, Danilov S, Macrander A, Ivanciu I (2020) Ocean bottom pressure variability: can it be reliably modeled? *J Geophys Res Oceans*. <https://doi.org/10.1029/2019JC015469>
- Araki E, Saffer DM, Kopf AJ, Wallace LM, Kimura T, Machida Y, Ide S, Davis E (2017) Recurring and triggered slow-slip events near the trench at the Nankai Trough subduction megathrust. *Science* 356(6343):1157–1160. <https://doi.org/10.1126/science.aan3120>
- Ariyoshi K, Iinuma T, Nakano M, Kimura T, Araki E, Machida Y, Sueki K, Yada S, Nishiyama T, Suzuki K, Hori T, Takahashi N, Kodaira S (2021) Characteristics of slow slip event in March 2020 revealed from borehole and DONET observatories. *Front Earth Sci Solid Earth Geophys*. <https://doi.org/10.3389/feart.2020.600793>
- Baba T, Tanioka Y, Cummins P, Uhira K (2002) The slip distribution of the 1946 Nankai earthquake estimated from tsunami inversion using a new plate model. *Phys Earth Planet Inter* 132:59–73. [https://doi.org/10.1016/S0031-9201\(02\)00044-4](https://doi.org/10.1016/S0031-9201(02)00044-4)
- Bürgmann R, Chadwell D (2014) Seafloor geodesy. *Ann Rev Earth Planet Sci* 42:509–534. <https://doi.org/10.1146/annurev-earth-060313-054953>
- Dobashi Y, Inazu D (2021) Improving detectability of seafloor deformation from bottom pressure observations using numerical ocean models. *Front Earth Sci Solid Earth Geophys*. <https://doi.org/10.3389/feart.2020.598270>
- Fredrickson E, Wilcock W, Schmidt D, MacCready P, Roland E, Kurapov A, Zumberge M, Sasagawa G (2019) Optimizing seafloor configurations for the detection of slow-slip earthquakes in seafloor pressure records, using the Cascadia subduction zone as a case study. *J Geophys Res: Solid Earth* 124:13504–13531. <https://doi.org/10.1029/2019JB018053>
- Fredrickson E, Gomberg J, Wilcock W, Hautala S, Hermann A, Johnson H (2023) Slow slip detectability in seafloor pressure records offshore Alaska. *J Geophys Res Solid Earth*. <https://doi.org/10.1029/2022JB024767>
- Fritsch F, Carlson R (1980) Monotone piecewise cubic interpolation. *SIAM J Numer Anal* 17:238–246. <https://doi.org/10.1137/0717021>
- Fukao Y, Kubota T, Sugioka H, Ito A, Tonegawa T, Shiobara H, Yamashita M, Saito T (2021) Detection of “rapid” aseismic slip at the Izu-Bonin Trench. *J Geophys Res Solid Earth*. <https://doi.org/10.1029/2021JB022132>
- Gomberg J, Hautala S, Johnson P, Chiswell S (2019) Separating sea and slow slip signals on the seafloor. *J Geophys Res: Solid Earth* 124:13486–13503. <https://doi.org/10.1029/2019JB018285>
- Hanawa K, Mitsudera F (1985) On the data processings of daily mean values of oceanographical data: note on the daily mean sea-level data. *Bull Coast Oceanogr* 23:79–87. [https://doi.org/10.32142/engankaio.23.1\\_79](https://doi.org/10.32142/engankaio.23.1_79) [in Japanese]
- Hasegawa T, Nagano A, Matsumoto H, Ariyoshi K, Wakita M (2019) El Niño-related sea surface elevation and ocean bottom pressure enhancement associated with the retreat of the Oyashio southeast of Hokkaido, Japan. *Mar Geophys Res* 40:505–512. <https://doi.org/10.1007/s11001-019-09392-8>
- Hasegawa T, Nagano A, Ariyoshi K, Miyama T, Matsumoto H, Iwase R, Wakita M (2021) Effect of ocean fluid changes on pressure on the seafloor: Ocean assimilation data analysis on warm-core rings off the southeastern coast of Hokkaido, Japan on an interannual timescale. *Front Earth Sci Solid Earth Geophys*. <https://doi.org/10.3389/feart.2021.600930>
- Hino R, Inazu D, Ohta Y, Ito Y, Suzuki S, Iinuma T, Osada Y, Kido M, Fujimoto H, Kaneda Y (2014) Was the 2011 Tohoku-Oki earthquake preceded by aseismic preslip? Examination of seafloor vertical deformation data near the epicenter. *Mar Geophys Res* 35:181–190. <https://doi.org/10.1007/s11001-013-9208-2>
- Hino R, Kubota T, Chikasada N, Ohta Y, Otsuka H (2022) Assessment of S-net seafloor pressure data quality in view of seafloor geodesy. *Prog Earth Planet Sci* 9:73. <https://doi.org/10.1186/s40645-022-00526-y>
- Hirose F, Nakajima J, Hasegawa A (2008) Three-dimensional seismic velocity structure and configuration of the Philippine Sea slab in southwestern Japan estimated by double-difference tomography. *J Geophys Res: Solid Earth* 113:B09315. <https://doi.org/10.1029/2007JB005274>
- Ide S, Beroza G, Shelly D, Uchide T (2007) A scaling law for slow earthquakes. *Nature* 447:76–79. <https://doi.org/10.1038/nature05780>
- Inazu D, Hino R, Fujimoto H (2012) A global barotropic ocean model driven by synoptic atmospheric disturbances for detecting seafloor vertical displacements from in situ ocean bottom pressure measurements. *Mar Geophys Res* 33:127–148. <https://doi.org/10.1007/s11001-012-9151-7>
- Inoue T, Ito Y, Wallace L, Yoshikawa Y, Inazu D, Garcia E, Muramoto T, Webb SC, Ohta K, Suzuki S, Hino R (2021) Water depth dependence of long-range correlation in nontidal variations in seafloor pressure. *Geophys Res Lett*. <https://doi.org/10.1029/2020GL092173>
- Ito Y, Hino R, Kido M, Fujimoto H, Osada Y, Inazu D, Ohzono M, Miura S, Mishina M (2013) Episodic slow slip events in the Japan subduction zone before the 2011 Tohoku-Oki earthquake. *Tectonophysics* 600:14–26. <https://doi.org/10.1016/j.tecto.2012.08.022>
- Iwasaki T, Sato H, Shinohara M, Ishiyama T, Hashima A (2015) Fundamental structure model of island arcs and subducted plates in and around Japan. 2015 Fall Meeting. American Geophysical Union, San Francisco, Dec 14–18:T31B-2878
- Jolliffe I (2002) Principal component analysis, 2nd edn. Springer, New York
- Kaneda Y, Kawaguchi K, Araki E, Matsumoto H, Nakamura T, Kamiya S, Ariyoshi K, Hori T (2015) Development and application of an advanced ocean floor network system for megathrust earthquakes and tsunamis. *Seafloor Observatories*, Springer Praxis Books, Springer, Berlin, Heidelberg
- Kawabe M (1985) Sea level variations at the Izu Islands and typical stable paths of the Kuroshio. *J Oceanogr Soc Japan* 41:307–326. <https://doi.org/10.1007/BF02109238>
- Kawaguchi K, Kaneko S, Nishida T, Komine T (2015) Construction of the DONET real-time seafloor observatory for earthquakes and tsunami monitoring. *Seafloor Observatories*, Springer Praxis Books, Springer, Berlin, Heidelberg
- Kositsky A, Avouac J (2010) Inverting geodetic time series with a principal component analysis-based inversion method. *J Geophys Res: Solid Earth* 115:B03401. <https://doi.org/10.1029/2009JB006535>
- Kubota T, Saito T, Fukao Y, Sugioka H, Ito A, Tonegawa T, Shiobara H, Yamashita M (2021) Earthquake rupture and tsunami generation of the 2015 MW5.9 Bonin event revealed by in situ pressure gauge array observations and integrated seismic and tsunami wave simulation. *Geophys Res Lett*. <https://doi.org/10.1029/2021GL095915>
- Kundu P, Allen J, Smith R (1975) Modal decomposition of the velocity field near the Oregon coast. *J Phy Oceanogr* 5:683–704. [https://doi.org/10.1175/1520-0485\(1975\)005%3c0683:MDOTVF%3e2.0.CO;2](https://doi.org/10.1175/1520-0485(1975)005%3c0683:MDOTVF%3e2.0.CO;2)
- Kutzbach J (1967) Empirical eigenvectors of sea-level pressure, surface temperature and precipitation complexes over North America. *J Appl Meteorol Climatol* 6:791–802. [https://doi.org/10.1175/1520-0450\(1967\)006%3c0791:EEOSLP%3e2.0.CO;2](https://doi.org/10.1175/1520-0450(1967)006%3c0791:EEOSLP%3e2.0.CO;2)
- Matsumoto H, Araki E (2021) Drift characteristics of DONET pressure sensors determined from in-situ and experimental measurements. *Front Earth Sci Solid Earth Phy* 8:600966. <https://doi.org/10.3389/feart.2020.600966>
- Menemenlis D, Campin J, Heimbach P, Hill C, Lee T, Nguyen A, Schodlok M, Zhang H (2008) ECCO2: high resolution global ocean and sea ice data synthesis. *Mercator Ocean Quarterly Newsletter* 31:13–21
- Munekane H (2012) Coseismic and early postseismic slips associated with the 2011 off the Pacific coast of Tohoku Earthquake sequence: EOF analysis of GPS kinematic time series. *Earth Planets Space* 64:3. <https://doi.org/10.5047/eps.2012.07.009>
- Muramoto T, Ito Y, Inazu D, Wallace L, Hino R, Suzuki S, Webb S, Henrys S (2019) Seafloor crustal deformation on ocean bottom pressure records with nontidal variability corrections: application to Hikurangi Margin, New Zealand. *Geophys Res Lett* 46:303–310. <https://doi.org/10.1029/2018GL080830>
- Nagano A, Yamashita Y, Hasegawa T, Ariyoshi K, Matsumoto H, Shinohara M (2019) Characteristics of an atypical large-meander path of the Kuroshio current south of Japan formed in September 2017. *Mar Geophys Res* 40:525–539. <https://doi.org/10.1007/s11001-018-9372-5>
- Nagano A, Yamashita Y, Ariyoshi K, Hasegawa T, Matsumoto H, Shinohara M (2021) Seafloor pressure change excited at the northwest corner of the Shikoku Basin by the formation of the Kuroshio large-meander in September 2017. *Front Earth Sci Solid Earth Phy* 8:583481. <https://doi.org/10.3389/feart.2020.583481>
- Nitani H (1972) Beginning of the Kuroshio. In: Stommel H, Yoshida K (eds) *Kuroshio-its physical aspects*. University of Tokyo Press, Tokyo, Japan, pp 129–163
- Nuryanto D (2016) A complex empirical orthogonal function for combining two different variables over Indonesian maritime continent. *AIP Conf Proc* 10(1063/1):4940844

- Obara K, Kato A (2016) Connecting slow earthquakes to huge earthquakes. *Science* 353:253–257. <https://doi.org/10.1126/science.aaf1512>
- Ohta Y, Hino R, Inazu D, Ohzono M, Ito Y, Mishima M, Iinuma T, Nakajima J, Osada Y, Suzuki K, Fujimoto H (2012) Geodetic constraints on afterslip characteristics following the March 9, 2011, Snariku-oki earthquake. *Japan Geophys Res Lett* 39:L16304. <https://doi.org/10.1029/2012GL052430>
- Okada Y (1992) Internal deformation due to shear and tensile faults in a half-space. *Bull Seis Soc Am* 75:1135–1154. <https://doi.org/10.1785/BSSA0820021018>
- Okada Y, Nishimura T, Tabei T, Matsushima T, Hirose H (2022) Development of a detection method for short-term slow slip events using GNSS data and its application to the Nankai subduction zone. *Earth Planets Space* 74:18. <https://doi.org/10.1186/s40623-022-01576-8>
- Polster A, Fabian M, Villinger H (2009) Effective resolution and drift of Paroscientific pressure sensors derived from long-term seafloor measurements. *Geochem, Geophys, Geosystems* 10:Q08008. <https://doi.org/10.1029/2009GC002532>
- Qiu B, Miao W (2000) Kuroshio path variations south of Japan: bimodality as a self-sustained internal oscillation. *J Phy Oceanogr* 30:2124–2137. [https://doi.org/10.1175/1520-0485\(2000\)030%3c2124:KPVSOJ%3e2.0.CO;2](https://doi.org/10.1175/1520-0485(2000)030%3c2124:KPVSOJ%3e2.0.CO;2)
- Roussel B, Campillo M, Lasserre C, Frank W, Cotte N, Walpersdorf A, Socquet A, Kostoglodov V (2017) A geodetic matched filter search for slow slip with application to the Mexico subduction zone. *J Geophys Res Solid Earth* 122:10498–10514. <https://doi.org/10.1002/2017JB014448>
- Sato T, Hasegawa S, Kono A, Shiobara H, Yagi T, Yamada T, Shinohara M, Usui N (2017) Detection of vertical motion during a slow-slip events off the Boso Peninsula, Japan, by ocean bottom pressure gauges. *Geophys Res Lett* 44:2710–2715. <https://doi.org/10.1002/2017GL072838>
- Sekine S, Hirose H, Obara K (2010) Along-strike variations in short-term slow slip events in the southwest Japan subduction zone. *J Geophys Res Solid Earth*. <https://doi.org/10.1029/2008JB006059>
- Suito H (2016) Detectability of interplate fault slip around Japan, based on GEONET daily solution F3. *J Geod Soc Japan* 62:109–120. <https://doi.org/10.11366/sokuchi.62.109> [in Japanese with English abstract]
- Suzuki K, Nakano M, Takahashi N, Hori T, Kamiya S, Araki E, Nakata R, Kaneda Y (2016) Synchronous changes in the seismicity rate and ocean-bottom hydrostatic pressures along the Nankai trough: a possible slow slip event detected by the Dense Oceanfloor Network system for Earthquakes and Tsunamis (DONET). *Tectonophysics* 680:90–98. <https://doi.org/10.1016/j.tecto.2016.05.012>
- Takagi R, Uchida N, Obara K (2019) Along-strike variation and migration of long-term slow slip events in the western Nankai subduction zone, Japan. *J Geophys Res: Solid Earth* 124:3853–3880. <https://doi.org/10.1029/2018JB018037>
- Tamura Y, Sato T, Ooe M, Ishiguro M (1991) A procedure for tidal analysis with a Bayesian information criterion. *Geophys J Int* 104:507–516. <https://doi.org/10.1111/j.1365-246X.1991.tb05697.x>
- Thompson R (1983) Low-pass filters to suppress inertial and tidal frequencies. *J Phy Oceanogr* 13:1077–1083. [https://doi.org/10.1175/1520-0485\(1983\)013%3c1077:LPTS%3e2.0.CO;2](https://doi.org/10.1175/1520-0485(1983)013%3c1077:LPTS%3e2.0.CO;2)
- Thomson R, Emery W (2014) Data analysis methods in physical oceanography. Elsevier B. V., Amsterdam
- Tsushima H, Hino R, Tanioka Y, Imamura F, Fujimoto H (2012) Tsunami waveform inversion incorporating permanent seafloor deformation and its application to tsunami forecasting. *J Geophys Res: Solid Earth* 117:B03311. <https://doi.org/10.1029/2011JB008877>
- Wallace L, Webb S, Ito Y, Mochizuki K, Hino R, Henrys S, Schwartz S, Sheehan A (2016) Slow slip near the trench at the Hikurangi subduction zone, New Zealand. *Science* 352:701–704. <https://doi.org/10.1126/science.aaf2349>
- Watts D, Kontoyiannis H (1990) Deep-ocean bottom pressure measurement: Drift removal and performance. *J Atmos Ocean Technol* 7:296–306. [https://doi.org/10.1175/1502-0426\(1990\)007%3c0296:DOBPMD%3e2.0.CO;2](https://doi.org/10.1175/1502-0426(1990)007%3c0296:DOBPMD%3e2.0.CO;2)
- Watts D, Wei M, Tracey K, Donohue K, He B (2021) Seafloor geodetic pressure measurements to detect shallow slow slip events: Methods to remove contributions from ocean water. *J Geophys Res Solid Earth*. <https://doi.org/10.1029/2020JB020065>
- Wells D, Coppersmith K (1994) New empirical relations among magnitude, rupture length, rupture width, rupture area, and surface displacement. *Bull Seis Soc Am* 84:974–1002. <https://doi.org/10.1785/BSSA0840040974>
- Wessel P, Smith W, Scharroo R, Luis J, Wobbe F (2013) Generic mapping tools: improved version released. *EOS Transactions* 94:409–410. <https://doi.org/10.1002/2013EO450001>
- Woods K, Webb S, Wallace L, Ito Y, Collins C, Palmer N, Hino R, Savage M, Saffer D, Davis E, Barker D (2022) Using seafloor geodesy to detect vertical deformation at the Hikurangi subduction zone: Insights from self-calibrating pressure sensors and ocean general circulation models. *J Geophys Res Solid Earth*. <https://doi.org/10.1029/2022JB023989>
- Yokota Y, Ishikawa T (2020) Shallow slow slip events along the Nankai Trough detected by GNSS-A. *Sci Adv*. <https://doi.org/10.1126/sciadv.aay5786>

## Publisher's Note

Springer Nature remains neutral with regard to jurisdictional claims in published maps and institutional affiliations.

**Hideto Otsuka** H.O. is a graduate student at the Graduate School of Science, Tohoku University.

**Yusaku Ohta** Y.O. is an associate professor at the Graduate School of Science, Tohoku University.

**Ryota Hino** R.H. is a professor at the Graduate School of Science, Tohoku University.

**Tatsuya Kubota** T.K. is a chief researcher at the National Research Institute for Earth Science and Disaster Resilience.

**Daisuke Inazu** D.I. is an associate professor at Tokyo University of Marine and Technology.

**Tomohiro Inoue** T.I. is a research fellow at Institute of Industrial Science, The University of Tokyo.

**Narumi Takahashi** N.T. is a principal chief researcher at National Research Institute for Earth Science and Disaster Resilience and a principal researcher at Japan Agency for Marine-Earth Science and Technology.

Submit your manuscript to a SpringerOpen® journal and benefit from:

- Convenient online submission
- Rigorous peer review
- Open access: articles freely available online
- High visibility within the field
- Retaining the copyright to your article

Submit your next manuscript at ► [springeropen.com](https://www.springeropen.com)